Coordination Chemistry Reviews 434 (2021) 213780

Contents lists available at ScienceDirect

Coordination Chemistry Reviews

journal homepage: www.elsevier.com/locate/ccr

Review

Metal-organic frameworks and their derivatives-modified photoelectrodes for photoelectrochemical applications

Meiying Jia [a,b], Weiping Xiong [a,b,*], Zhaohui Yang [a,b,*], Jiao Cao [a,b], Yanru Zhang [a,b], Yinping Xiang [a,b], Haiyin Xu [c], Peipei Song [d], Zhengyong Xu [e]

[a] College of Environmental Science and Engineering, Hunan University, Changsha 410082, PR China
[b] Key Laboratory of Environmental Biology and Pollution Control (Hunan University), Ministry of Education, Changsha 410082, PR China
[c] College of Environmental Science and Engineering, Central South University of Forestry and Technology, Changsha 410004, PR China
[d] College of Resources and Environment, Key Laboratory of Agricultural Environment, Shandong Agricultural University, Taian 271000, PR China
[e] Hunan Provincial Science and Technology Affairs Center, Changsha 410013, PR China

ARTICLE INFO

Article history:
Received 31 July 2020
Accepted 6 January 2021

Keywords:
Metal-organic frameworks
Photoelectrode
Photo-electrochemistry applications
Water splitting
Photo-electrochemical sensor

ABSTRACT

Artificial photosynthesis based on photoelectrochemical (PEC) strategy is another solar-to-chemical energy conversion method besides photocatalysis. Owing to the diversity of structure and the adjustability of synthesis, the metal-organic frameworks (MOFs) can enrich this important research field in the form of constructing a photoelectrode. In addition to solving the problems of difficult recovery for powder and the easy recombination for carriers in photocatalysis, MOFs and their derivatives-modified photoelectrodes can reasonably adjust the PEC activity at the molecular level and increase the contact area between the electrolyte and electrode, thereby facilitating the diffusion of electrolyte and reaction substrate in the electrode. In this review, we comprehensively reviewed representative studies in this area. Firstly, functions of MOFs in photoelectrodes are outlined, and the various synthesis strategies of MOFs-modified photoelectrodes are elaborated. Subsequently, special attention has been paid to the application and mechanism of MOFs-modified photoelectrodes (MIL, ZIF, UiO and PCN) in photo-electrochemistry. And we discuss the stability, reproducibility and reusability of MOFs-modified photoelectrodes. Finally, the challenges and improvements of MOFs-modified photoelectrodes in promoting practical application are proposed. Overall, MOFs and their derivatives-modified photoelectrodes achieved the integration of adsorption, photocatalysis and electrocatalysis. Notably, the research in this field is in infancy, many improvements are required before practical applications.

Contents

* Corresponding authors at: College of Environmental Science and Engineering, Hunan University, Changsha, Hunan 410082, PR China.
E-mail address: xiongweiping@hnu.edu.cn (W. Xiong).

https://doi.org/10.1016/j.ccr.2021.213780
0010-8545/

1. Introduction

The shortage of energy supply and the increase of environmental pollution caused by the increase in energy consumption have become major challenges for the world in the 21 st century [1–3]. According to the World Energy Technology Outlook-2050 prediction, world energy consumption is estimated to be approximately double from 10 Gtoe today to about 22 Gtoe in 2050 [4]. The green energy utilization method has been utilized to address the energy crisis [5–7]. In nature, the photosynthesis of chloroplast can convert solar energy photochemistry into chemical energy. Similar to natural photosynthesis, energy conversion has attracted more attention from the scientific community [8–10]. To develop more ways to use sustainable energy, artificial photosynthesis, which converts CO_2 and H_2O into high-value-added carbon products or clean H_2 fuel by using sunlight, [11–13] is gradually being used to respond to sustainable development strategies. For a long time, the use of solar energy has been an indispensable research topic [14–16]. As early as 1970 s, Fujishima and Honda first explored the photoelectrochemical (PEC) water splitting technology, which combined solar energy with electrical energy to output chemical energy more efficiently [17]. The PEC water splitting process effectively combined the renewable energy required by the photocatalytic system with electrocatalysis, and thus obtaining higher catalytic efficiency.

PEC systems are hybrids of PV and EC systems, and they are generally composed of two electrodes immersed in the electrolyte and an external power supply. Among them, at least one electrode must be a semiconductor material or semiconductor-like material to be used as a photoanode or photocathode [18]. And the electrode should have the functions of light-harvesting and electrocatalysis simultaneously. The high efficiency of PEC progress is attributed to the directed migration and rapid conduction of photogenerated electrons by the external circuit, which effectively suppresses the recombination of electron-hole pairs (e^-/h^+ pairs) [19]. Since the photoelectrode is a key part of the entire energy conversion process, the efficiency of the PEC system is strictly limited by the structure of the photoelectrode. Generally, the researches of the photoelectrodes are focused on the construction of photoanode via n-type semiconductor for the oxidation reaction and the construction of photocathode via the p-type semiconductor for the reduction reaction [20]. In the construction process of photoelectrodes, inorganic semiconductor materials are often used as the electrode substrate. It must be mentioned that most semiconductors such as TiO_2, $BiVO_4$, Cu_2O, Fe_2O_3, still suffer many challenges, such as poor light collection performance, low electron-hole separation efficiency, inappropriate absorption band gap, and low catalytic activity (Table 1). After more than a decade of development, coordination polymers have obtained considerable attention due to their novel functions and exquisite structural units [21–23]. Among them, as a kind of coordination polymers with permanent porosity, metal-organic frameworks (MOFs) have developed rapidly and are developed to meet many challenges in the field of biological, energy and environment, such as gas separation, [24–26] organic pollutants adsorption, [27,28] catalytic reactions, [29–32] chemical sensing, [33,34] biomedical, [35–38] and gas storage [39–42]. In the construction of the novel photoelectrode, regular structured MOFs exhibit outstanding synthesis adjustability due to the changeable organometallic ions or clusters and flexible organic ligands, [43–47] which is beneficial to meet the needs of traditional photo-electronic materials modification and PEC performance improvement. In addition, after combined with specific heat treatment, MOFs can further adjust their chemical composition and their derived nanostructures can maintain regular porosity and high surface area, [48–52] which accelerate electrolyte into the electrode and form an increased contact area between electrolyte and electrode. Therefore, MOFs and their derivatives are considered as the ideal platform for solving the challenges encountered in PEC systems.

As early as 2012, Hou et al. [53] had reported for the first time that the MOFs thin film was deposited uniformly on the glassy carbon electrode (GCE), and provided insights on the application of the MOFs thin film as a PEC sensor. They used 4-carboxyphenyldiazonium salt to modify GCE and thus introduc-

Table 1
The properties and modification strategies of common semiconductors.

Sample	Band gap	Advantage	Disadvantage	Modified strategy
TiO_2	3.0–3.2 eV	Wide chemical stability	Low charge carrier mobility	Doping-deposition
		Large availability	Narrow absorption range	Doping-sensitization
		Photocatalytic activity	High electrical resistivity	Deposition-coupling
$BiVO_4$	2.4–2.5 eV	Crystal structure stability	Low specific surface area	Nanostructure modification
		High light quantum	Poor quantum utilization	Surface engineering
		e^- transmission efficiency	Low e^-/h^+ separation efficiency	Heterojunction
Cu_2O	2.0–2.2 eV	High hole-mobility	Low stability	Co-catalyst deposition
		Non-tox	Light corrosion	Tuning crystal facets
		Generally abundant	Much grain boundary defect states	Atomic layer deposition
Fe_2O_3	2.1–2.2 eV	Recyclability	Indirect band gap transitions	Nanostructure design
		Excellent earth-abundant	Short excited-state lifetime 10–12 s	Z-scheme heterojunction
		Harvesting of visible light	Short hole diffusion length 2–4 nm	Heteroatoms doping

ing carboxyl groups into the surface of GCE, which solved the problem of poor hetero-nucleation of MOFs crystals on supports. The preparation method of the MOFs thin film gave important guidance for expanding the application of other materials as supports. Simultaneously, due to the self-assembled monomolecular (SAM) could interact specifically with metal-cluster secondary-building unit, the research team used 3-aminopropyltriethoxysilane (APTES) as the SAM and prepared a (1 1 0) oriented ZIF-8 thin film on the APTES functionalized indium tin oxide (ITO) electrode [54]. The research of this highly oriented ZIF-8 thin film on electrode was once again laid the basis of MOFs thin film in PEC applications. Up to now, although the researches on MOFs photoelectrodes is limited, it has performed well in many PEC applications. For example, Zhang et al. [44] used aminated titanium-based MOFs-sensitized TiO_2 nanowire as a photoanode for solar water splitting in 2016, which successfully increased the photocurrent to nearly 100% under visible light. At the same time, Sun et al. [55] used ZIF-8-derived carbonaceous material as the counter electrode in dye-sensitized solar cells, and the results showed that the efficiency of the obtained the solar cell based on carbonaceous materials was 7.32% under the illumination of Air-Mass (AM) 1.5G, which was comparable to that based on Pt electrode under the same conditions. In addition, in terms of PEC reduction of CO_2, Deng et al. [56] developed a new type of photocathode formed by coating MOFs ($Cu_3(BTC)_2$) on the surface of Cu_2O photocathode in 2019. The ideal interface formed on the Cu_2O substrate promoted the transfer of electrons from the Cu_2O substrate to the surface of MOFs layer to achieve enhanced PEC-CO_2 release.

In recent years, the researches on the application of MOFs in photo-electrochemistry has made many innovative achievements, it is necessary to summarize the research progress of MOFs in photo-electrochemistry and thus laying the research foundation in this field. Unfortunately, there is little review on the use of MOFs and their derivatives-modified photoelectrodes for PEC applications. According to our search, in 2019, Deng et al.'s review entitled Metal-organic frameworks for artificial photosynthesis via photoelectrochemical route" is the only review on the PEC applications of MOFs, [20] but this review only summarized some research results on the advancement of light collection performance, the improvement of charge dynamics and the promotion of co-catalyst for MOFs-modified photoelectrodes. In this review, the state of the developments in this field will be more comprehensively summarized. We begin by reviewing the MOFs-modified photoelectrodes construction principles and forming method. Subsequently, we compare the PEC applications of common MOFs series in photoelectrodes, including Materials of institute Lavoisier (MIL), Zeolitic imidazole frameworks (ZIF), University of Oslo (UiO) and Porous coordination network (PCN). And we discusse the stability, reproducibility and reusability of MOFs-modified photoelectrodes. In the end, we propose the future prospect with remaining challenges. Toward the future development of MOFs-modified photoelectrodes in artificial photosynthesis, this review is aimed to elaborate the essential features and basic concepts involving constructing MOFs and their derivatives-modified photoelectrodes and optimizing the relevant performance, thereby expanding the application of MOFs in photo-electrochemistry.

2. Functions of MOFs in photoelectrodes

In the process of forming PEC devices, MOFs play significant roles in improving the efficiency and practicability of photoelectrodes, which are mainly represented from the following aspects: (i) enhancing light harvesting capability, the light absorption range is expanded; (ii) accelerating carrier separation efficiency, the circuit-assisted separation is improved; (iii) increasing charge injection efficiency, the heterogeneous interface mass transportation is enhanced; (iv) optimizing the photoelectrode structure, the catalytic activity of heterojunction is improved.

2.1. Improving light utilization efficiency

In the research of PEC system, light utilization efficiency is the primary factor affecting solar energy conversion efficiency. Improving light utilization efficiency as much as possible plays an important role in improving the performance of photoelectrodes. Oxides have different light utilization efficiency due to different inherent band gaps. TiO_2 exhibits a wide band gap (3.0–3.2 eV) and low light utilization efficiency, [57–65] but it occupies an important position in the exploration of photoelectrode mechanism due to its diverse morphology, good stability, and high chemical activity. Considering the controllable band gap and light absorption, MOFs are considered to be an effective photosensitizer [44,66]. For example, Song et al. [67] used solvothermal method to decorate NH_2-MIL-125 (Ti) nanoparticles (NPs) into an ordered channel array of TiO_2 nanotubes (NTs) and fabricated TiO_2-NTs@Ti-MOF composite electrode to apply as an anode in photocatalysis. The maximum absorption peak of pure TiO_2-NTs appeared at 392 nm, and after compounding with Ti-MOF, the absorption peak extended to 481 nm. Correspondingly, the band gap of the composite electrode was also shortened from 3.2 eV of pure TiO_2-NTs to 2.3 eV. The results indicated that the heterogeneous band structure constructed by MOFs and semiconductors is accompanied by excellent light utilization efficiency. Also with wide band gap is ZnO (3.37 eV), Zhou et al. [68] successfully used MOFs derivatives as photosensitizers to improve the light utilization efficiency. They first grown ZIFs in situ on semiconductor ZnO. In order to obtain huge surface area shells and rich porosity, they sulfurized ZnO@Zn-ZIF, ZnO@Co-ZIF, and ZnO@ZnCo-ZIF. Finally, they obtained honeycomb ZnO@ZnS, ZnO@CoS and ZnO@ZnS/CoS heterojunction photoelectrodes, respectively (Fig. 1a). The structural properties after vulcanization provided long incident photon transmission pathways and abundant exposed active sites to achieve effective light absorption. As shown in the ultraviolet–visible spectrum (UV–vis) (Fig. 1b), compared with the original ZnO photoelectrode, the sulfide MOFs promoted the photoelectrode spectrum to red-shift in different degrees. Under full-spectrum illumination, the PEC performance of ZnO@ZnS/CoS was far superior to the previously reported ZnO-based photoanode [69–71].

Different from TiO_2 and ZnO, $BiVO_4$ (2.4–2.5 eV) gradually play an increasingly important role in the research of PEC systems due to the appropriate band gaps. In order to further improving the light utilization, MOFs are also used as photosensitizers to extend the absorption of visible light. Liu et al. [72] prepared an ultra-thin MIL-101 (Fe) layer on the surface of Mo: $BiVO_4$ by a hydrothermal method to construct a core–shell structured photoanode. The UV–vis spectrum (Fig. 1c) showed that the UV–vis spectra of the original $BiVO_4$ and Mo: $BiVO_4$ little difference in the spectra edge. However, after the introduction of MIL-101 (Fe), the light absorption of the photoanode in the visible light region was significantly improved. This indicated that the visible light responses of the organic ligands and Fe-O clusters in the MIL-101 (Fe) structure effectively changed the band gap of $BiVO_4$ and expanded the photoelectrode's absorption of visible light.

2.2. Accelerating carrier separation efficiency

Ensuring that the photogenerated e^-/h^+ pairs are separated and transferred to the active site is an essential strategy to improve the PEC efficiency of photoelectrodes. By changing the building blocks of MOFs, the highest occupied molecular orbital (HOMO) and lowest unoccupied molecular orbital (LUMO) energy levels can be

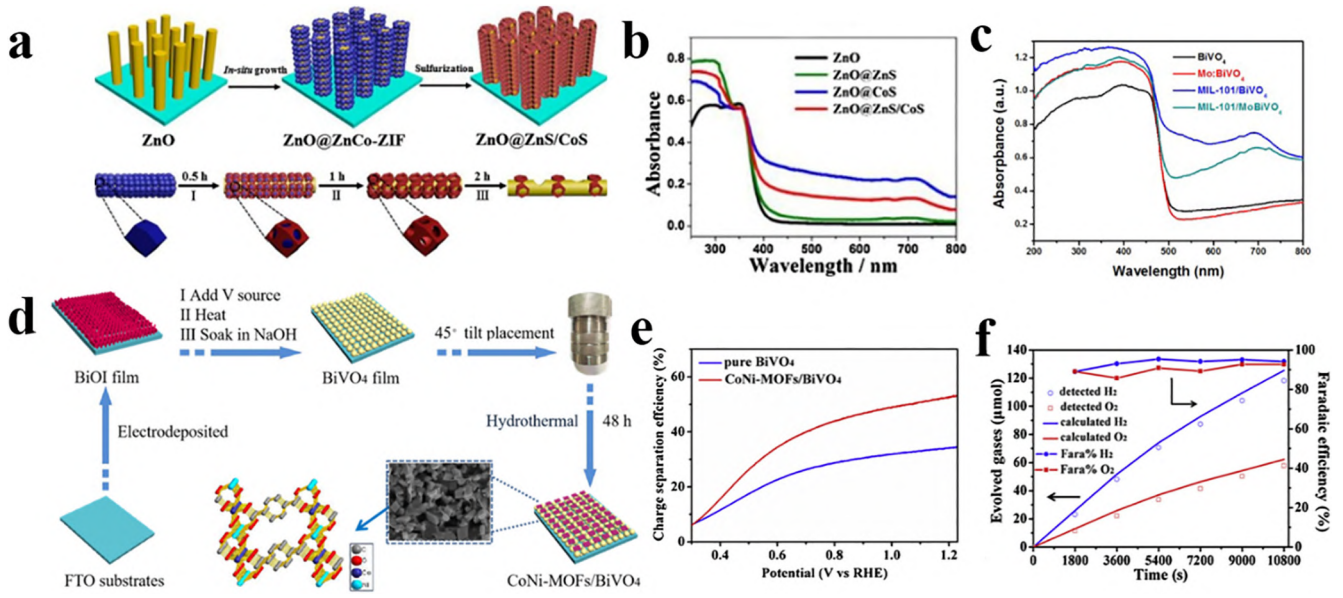

Fig. 1. (a) Schematic illustration for the fabrication and the formation process of cellular ZnO@ZnS/CoS. (b) The UV–vis diffuse reflectance of ZnO, ZnO@ZnS, ZnO@CoS, and ZnO@ZnS/CoS. (a-b) are reproduced with permission from Ref. [68]. Copyright 2018 Elsevier. (c) UV–vis spectra of $BiVO_4$, MIL-101(Fe)/$BiVO_4$, Mo: $BiVO_4$ and MIL-101(Fe)/Mo: $BiVO_4$ photoanodes. Reproduced with permission from Ref. [72]. Copyright 2020 Elsevier. (d) Schematic illustration of CoNi-MOFs/$BiVO_4$. (e) Charge separation efficiency of $BiVO_4$ and CoNi-MOFs/$BiVO_4$. (f). Evolution of H_2 and O_2 gases compared with the evolution expected from the current generation and the faradaic efficiency. (d-f) are reproduced with permission from Ref. [116]. Copyright 2020 Elsevier.

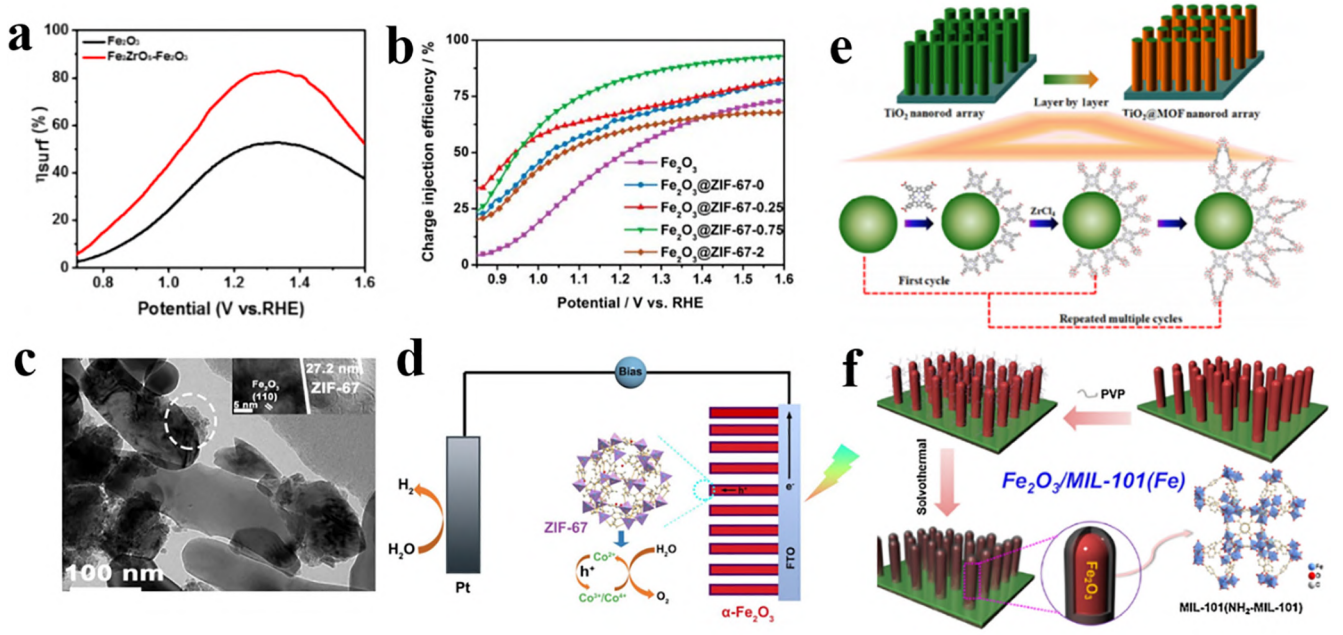

Fig. 2. (a) Charge separation efficiencies (η_{surf}) of Fe_2O_3 and Fe_2ZrO_5-Fe_2O_3. Reproduced with permission from Ref. [74]. Copyright 2020 Elsevier. (b) Charge injection efficiencies for the different samples. (c) TEM and HR-TEM images of Fe_2O_3@ZIF-67. (d) A proposed mechanism of PEC water oxidation for Fe_2O_3@ZIF-67 composite. (b-d) are reproduced with permission from Ref. [81]. Copyright 2019 Elsevier. (f) Scheme for the synthesis of TiO_2@MOF nanorod array photoanode through layer-by-layer method. Reproduced with permission from Ref. [82]. Copyright 2019 Springer. (g) Schematic of the synthesis process of Fe_2O_3/MIL-101(Fe) core/shell film on FTO substrate via surfactant-assisted solvothermal method. Reproduced with permission from Ref. [66]. Copyright 2018 Elsevier.

adjusted to better match semiconductor energy level and transport carriers [20]. In addition, proper selection of organic ligands and metal centers can also increase the charge carrier mobility of MOFs, and thus partially avoiding photo-corrosion and improving incident photon-electron conversion efficiency (IPCE). Recently, Zhou's group [73] proposed a strategy to improve the charge separation efficiency at the electrolyte/semiconductor interface by using bimetallic MOFs with variable valence. They used hydrothermal deposition method to deposit CoNi-MOFs uniformly on the surface of $BiVO_4$ (Fig. 1d), and obtained a binary photoanode composed of 3D bimetallic MOFs and $BiVO_4$. When irradiated by visible light, the holes generated by $BiVO_4$ after absorbing photons migrated to CoNi-MOFs, and Co^{2+} and Ni^{2+} captured the holes in time and were oxidized to higher valence states (Co^{3+}/Co^{4+} and

Ni^{3+}/Ni^{4+}). The high-valent metal ions subsequently became active sites to oxidize the interfacial H_2O to O_2. While the electrons were transferred to the counter electrode via the external circuit and participate in the water reduction reaction to generate H_2. Therefore, the photo-generated charges were effectively separated (Fig. 1e). As shown in Fig. 1f, the ratio of oxygen and hydrogen precipitated by CoNi-MOFs/$BiVO_4$ was close to the theoretical value, and the Faraday efficiency was about 90%, which further proved that in this PEC system, most of the photogenerated charges were separated in time to produce O_2 and H_2. Correspondingly, the IPCE of CoNi-MOFs/$BiVO_4$ had been improved, which was three times that of pure $BiVO_4$. In addition, Jiao and his colleagues [74] proposed a strategy for trapping defects in the passivation layer to improve the separation efficiency of e^-/h^+ pairs. Passivation layers were originally applied to semiconductor photoelectrodes to reduce corrosion and improve their chemical or photochemical stability when immersed in an electrolyte [75]. They used Zr-MOFs as a precursor to deposit a surface passivation layer-Fe_2ZrO_5 on hematite, which could passivate the surface defects and effectively decrease the electron-hole recombination [76–78]. The charge separation efficiency at the solid–liquid interface could thus be significantly enhanced [79]. The effect could be proved from the results of the surface charge separation efficiency of Fe_2ZrO_5-Fe_2O_3 (Fig. 2a). Compared with Fe_2O_3, Fe_2ZrO_5-Fe_2O_3 exhibited a higher surface charge separation efficiency. In addition to improving the efficiency of electron and hole separation, the effective surface passivation layer could further reduce the initial potential, thereby obtaining better PEC performance. Meanwhile, the Fe_2ZrO_5 layer could also provide Zr-doping in hematite, which would significantly increase the donor density and thus the electrical conductivity.

2.3. Increasing charge injection efficiency

The charge injection efficiency can intuitively reflect the influence of the photoelectrode on the reaction kinetics, thereby affecting the performance of photo-electrochemistry [80]. In 2019, Li and his colleagues [81] reported that the Fe_2O_3@ZIF-67 photoelectrode exhibited high charge injection efficiency. At 1.23 V vs reversible hydrogen electrode (RHE), the efficiency could reach 85%, which was 1.6 times that of Fe_2O_3 (Fig. 2b). The increased charge injection efficiency was attributed to unique electrode structure. Specifically, the ZIF-67 overlayer was encapsulated on the surface of Fe_2O_3 nanorod uniformly (Fig. 2c). When the excited photo-generated holes migrated from the valence band of Fe_2O_3 to ZIF-67, the ZIF-67 covering layer can effectively use the surface porous structure to guide the holes into the electrolyte (Fig. 2d), thereby improving the mass transfer ability of the heterogeneous interface. This was ultimately reflected in the enhancement of the charge injection efficiency from the photoanode surface to the electrolyte. Also for Co-MOF, Yang and others [82] also formed a TiO_2@Co-MOF photoanode by coating p-type porphyrin-based MOF on TiO_2 nanorod array (Fig. 2e). The TiO_2@Co-MOF photoanode was vertically arranged on Fluorine-doped tin oxide (FTO) electrical contacts, maintaining the long optical path-length of a few photo-generated carriers (holes) along the vertical axis of the nanorod, while allowing the short optical path-length of most photo-generated holes along the nanorod radius (transverse direction) to the photoanode/electrolyte interface. The enhancement of the charge injection efficiency owing to the porous surface with multiple reactive centers provided by the p-type MOF coating and the charge extraction rate of Co^{2+}.

2.4. Optimizing the photoelectrode structure

MOFs exhibit semiconductor-like properties, they can form heterojunctions with semiconductor substrates to enhance catalytic activity. Due to the synthetic adjustability of MOFs, the tightness, effective contact area and response sites of the electrodes formed by MOFs and semiconductor substrate can be effectively improved by controlling the thickness of the MOF layer and the size of the crystallites [81,83,84]. Dong et al. [66] used surfactant-polyvinylpyrrolidone (PVP) molecules as intermedia to controllably form ultra-thin MIL-101(Fe) shell on the surface of Fe_2O_3 nanorods (Fig. 2f). The semiconductor/MOFs core/shell heterostructure increased active sites and realized efficient water oxidation. During the growth of MOFs, PVP could serve as an end-capping agent to control the morphology of MOFs nanoparticles. And a tight connection between the nano-scale uniform MIL-101(Fe) shell and the Fe_2O_3 core was formed simultaneously. Finally, the synergistic effect of MOFs and hematite together resulted in superior PEC performance. The composite photoanode delivered a photocurrent density of 2.27 $mA{\cdot}cm^{-2}$ at 1.23 V vs. RHE, which was about 2.3 folds of that of pristine Fe_2O_3. Li et al. [81] developed similar research work. The research team also used PVP as intermedia to grow ZIF-67 on the surface of Fe_2O_3 nanorods. Through the polar groups (pyrrolidone ring) and non-polar groups, PVP could easily adsorbed on the solid surface, and thus enhancing the affinity between electrode and electrolyte by the coordination of the pyrrolidone ring and Co^{2+}. Finally, Fe_2O_3@ZIF-67 photoelectrode with excellent water oxidation performance was prepared, the evolution amount of H_2 was 12.5 $\mu mol{\cdot}cm^{-2}h^{-1}$, and O_2 was 5 $\mu mol{\cdot}cm^{-2}h^{-1}$.

3. The construction strategy of the PEC device

According to the way that the conductive substrate participates in the photoelectrode, we divide the construction strategy of the PEC device during photo-electrochemistry into the following three categories: (1) coating materials to form photoelectrodes; (2) growing materials to form photoelectrodes; (3) evolving materials to form photoelectrodes.

3.1. Coating materials to form photoelectrodes

The photoelectrode formed by coating material is constructed by dispersing the synthesized material into the solution, then coating and fixing it on the conductive substrate with adhesive, and the whole process is usually repeated 3–5 times, or even more. In this method, Nafion is used as adhesive and ITO is widely used as a conductive substrate due to the excellent optical and electrical properties [85]. As described in the method of Wang et al. [86] black titanium dioxide (B-TiO_2) dispersion, Bi_2O_3 dispersion and AuNPs was dropped onto the ITO to obtain the AuNPs/Bi_2O_3/B-TiO_2 photoelectrode. Bi_2O_3/B-TiO_2 nanocomposites were used as photoactive material, and the AuNPs could anchored the m^6A antibody. The $[Zr_6O_4(OH)_4]$ clusters in UiO-66 could strongly bind with phosphate groups. After capturing m^6A, UiO-66 specifically attached to the phosphate group of m^6A. In addition, the high porosity of UiO-66 facilitated the enrichment of $[Ru(bpy)_3]^{2+}$, and the excited state electrons generated by $[Ru(bpy)_3]^{2+}$ under visible light irradiation could be transferred to the Bi_2O_3/B-TiO_2/ITO photoelectrode to boost the photocurrent response. In the final PEC sensor (Fig. 3a), Ru@UiO-66 took the advantages of improving light collection efficiency and photoelectric conversion efficiency as the phosphate identification unit and signal amplification unit for detecting m^6A. Similarly, Gao et al. [87] coated CdS/Eu-MOF suspension on the ITO conductive glass surface to produce CdS/Eu-MOF composite electrode. Yang et al. [88] prepared a NPC-ZnO electrode by dropping NPC-ZnO nano-polyhedron suspension on the surface of the ITO conductive glass and drying it in air. Cao et al. [89] used Nafion to fix CuO on the surface of ITO and successfully prepared CuO/Cu-BTC electrode. Liu et al. [90] also used the method of

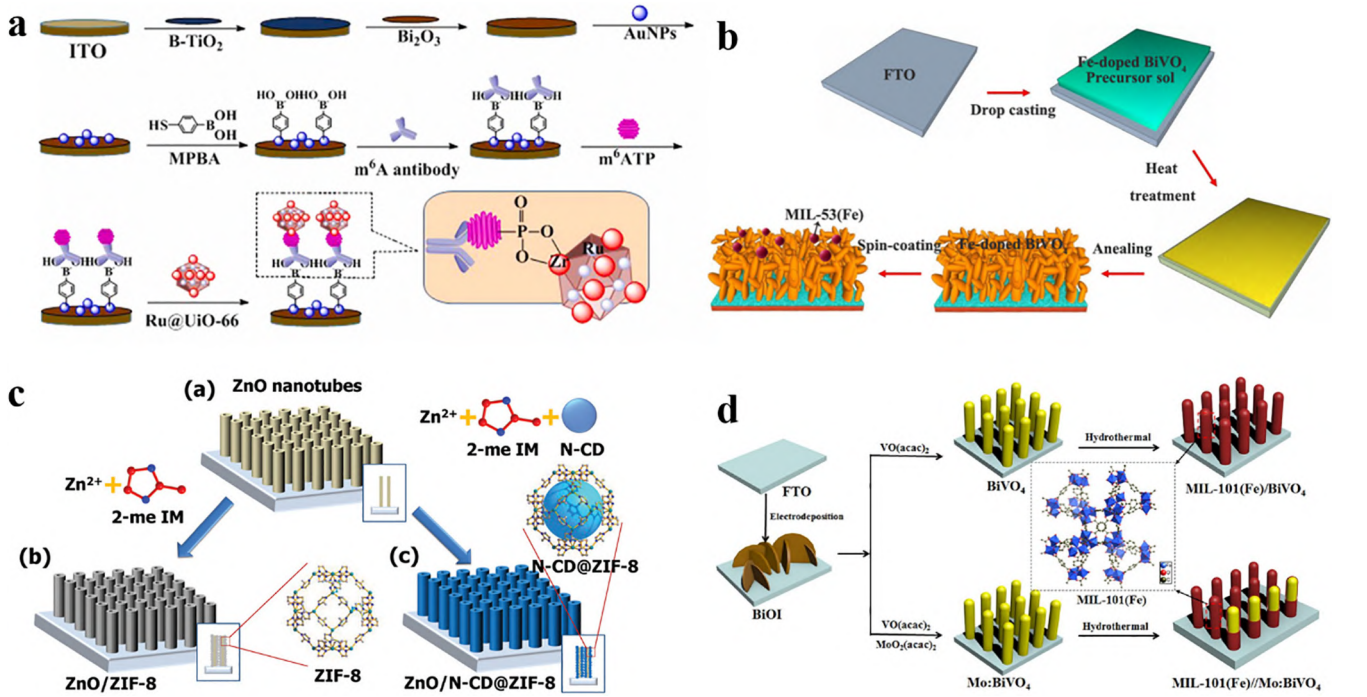

Fig. 3. (a) Schematic illustration of the fabrication procedure of the PEC immunosensor. Reproduced with permission from Ref. [86]. Copyright 2019 Elsevier. (b) Schematic illustration of the preparation process of Fe-doped $BiVO_4$ modified with MIL-53(Fe). Reproduced with permission from Ref. [90]. Copyright 2018 Elsevier. (c) Schematic illustrations of a) ZnO nanotubes, b) ZnO nanotubes with ZIF-8, and c) ZnO nanotubes with N-CD embedded ZIF-8. Reproduced with permission from Ref. [97]. Copyright 2019 Wiley. (d) Schematic of synthesis process of MIL-101(Fe)/$BiVO_4$ and MIL-101/Mo: $BiVO_4$ shell-core films on FTO glass substrate via PVP-assisted solvothermal method. Reproduced with permission from Ref. [72]. Copyright 2020 Elsevier.

dropping the precursor solution on the transparent conductive film to prepare the photoelectrode. Differently, the conductive substrate was lower cost FTO, and the electrode after coating and drying was further annealed at high temperature to obtain non-porous iron-doped semiconductor/MOFs electrode (Fig. 3b).

In addition to the transparent conductive film as a conductive substrate, sponge porous copper foam, nickel foam, etc., which also exhibit excellent conductivity, can also participate in the construction of the photoelectrode as conductive substrate. In addition to lower cost, the regularly spaced open-pore structures in the metal foam could provide a high specific surface area for redox coupling in the electrolyte and reduce the mass transfer limitations of the electrolyte in the electrode [91]. Among them, nickel foam has a unique three-dimensional porous structure, which is composed of three-dimensional interconnected metal pillars with pores, and exhibits electrical conductivity equivalent to that of metal foil. It allows metal foam to serve as a good electron transport substrate from the external circuit to the redox electrolyte when compared with ITO and FTO. In addition, the nickel foam is beneficial to electrodeposition, and allows the light to continuously refraction after passing through so as to use the light more effectively when compared with the mesh or plate structure [92]. Similarly, due to the 3D structure and high adsorption, copper foam is often used as a collector electrode [93]. In related research, Cheng and his colleagues [94] mixed C-Zn/Co-ZIF catalyst, Nafion and Deionized water (DI) together to coat on the foam copper. Copper foam was used as a 3D conductive support, which could uniformly disperse the C-Zn/Co-ZIF catalyst and effectively prevent the catalyst from agglomeration. The photocathode showed specific selectivity to high-end solar energy in PEC-CO_2 reduction.

3.2. Grow materials to form photoelectrodes

The photoelectrode formed by the coating method is simple and fast to construct. However, it may fall off because the interface between the material and the substrate has poor tightness, and the mass transfer rate will be affected. Therefore, effectively improving the mass transfer process has become a further research direction for constructing photoelectrodes. Recently, materials growing onto bare ITO/FTO surfaces have gradually become an area of concern. Rouby's research team [95] successfully obtained in-situ grown Titanium dioxide nanorod (TDNR) on the FTO conductive glass by hydrothermal method. They put the solution mixed with Titanium butoxide, HCl and DI together with FTO conductive glass into a stainless-steel autoclave lined with Teflon to obtain glass-FTO-TDNRs. Then, a dense and ultra-thin ZIF-8 film was anchored on the surface of glass-FTO-TDNRs substrate to achieve the in-situ modification of MOFs on the vertically oriented TiO_2 surface. Jia et al. [96] also placed the FTO conductive glass in the autoclave to obtain the FTO grown with ZnO@ZIF-8/67 nanorod arrays. Han et al. [97] combined hydrothermal and selective etching methods to prepare ZnO-NTs on FTO glass, and calcined the FTO substrate with ZnO-NTs in a 500 °C muffle furnace to remove the surfactant. Then put it again in autoclave equipped with a mixture of MOFs precursor and N-CD, with the conductive surface facing down. After layer-by-layer growth, ZnO/N-CD@ZIF-8 photoelectrode was obtained (Fig. 3c).

In addition to the traditional hydrothermal growth method, Kaur et al. [98] used electrodeposition to help the material grow on the FTO surface. They used TiO_2/FTO glass as the work electrode. Electrodeposited electrolyte was formed by single layer graphene aqueous dispersion and Eu-MOF/DMF dispersion. The graphene-MOF composite photoelectrode was obtained by immersing TiO_2/FTO in above solution and depositing it under constant applied potential. Liu and others [72] have recently completed a similar study. They used FTO as the working electrode and selected a KI solution, Bi $(NO_3)_3{\cdot}5H_2O$, and anhydrous ethanol containing p-benzoquinone as the electroplating solution of BiOI film. The chemical conversion of BiOI to $BiVO_4$ was then achieved by calcination (Fig. 3d) and the final MIL-101(Fe)/Mo: $BiVO_4$ photoanode was

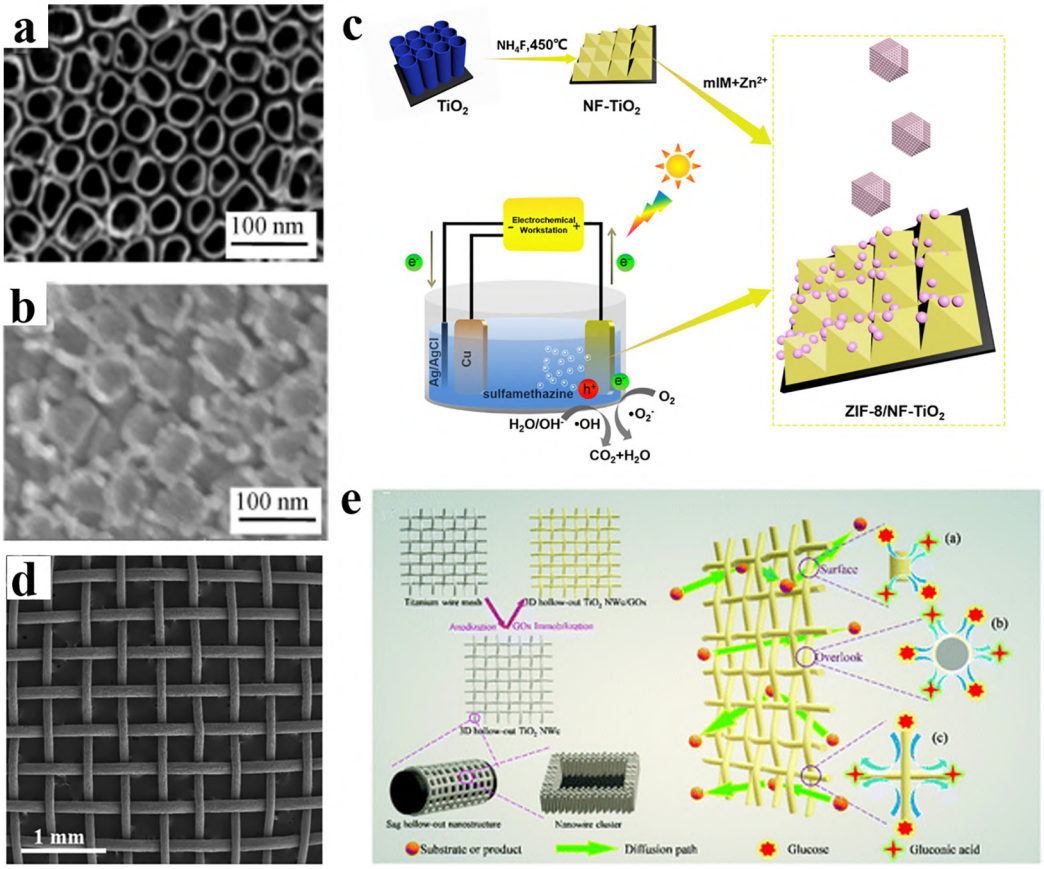

Fig. 4. SEM images of (a) TiO_2-NTs and (b) $Mn_3(BTC)_2$/g-C_3N_4/TiO_2-NTs. Reproduced with permission from Ref. [108]. Copyright 2017 Elsevier. (c) Schematic diagram of ZIF-8/NF-TiO_2 photoelectric catalytic removal of sulfamethazine. Reproduced with permission from Ref. [109]. Copyright 2020 Elsevier. (d) SEM image of 3D hollow-out TiO_2 NWc electrode. (e) Preparation process of the 3D hollow-out TiO_2 NWc/GOx electrode, insets (a)-(c) are intended to show that the space utilization of the enzymatic reaction can be extremely high. (d-e) are reproduced with permission from Ref. [101]. Copyright 2020 RSC.

obtained after doping with Mo and in-situ growing MOFs layer. The target photoelectrode not only increased the hole diffusion length but also improved the conductivity of photogenerated carriers. Ultimately, under simulated AM 1.5 G sunlight, the photocurrent density of the obtained photoanode in Na_2SO_4 aqueous solution could reach to 4.0 mA·cm^{-2} at 1.23 V vs RHE, which was about 4 times that of the $BiVO_4$ photoanode.

3.3. Evolving materials to form photoelectrodes

The above electrodes form body electrode by combining additional conductive substrate with synthetic material. The PEC behavior of the above electrodes is often limited by the performance of the conductive substrate. Fortunately, the evolution of the semiconductor itself to conductive substrate has solved the problem well. At present, the common semiconductor substrates in the research on constructing PEC devices are TiO_2.

TiO_2 has the advantages of low toxicity, high stability, and excellent catalytic activity. It participates in the construction of PEC devices in the form of nanotubes, [67,99] nanorods, [100] nanowires, [101] and nanoribbons [102,103]. The most popular form is the nanotubes structure, which is mainly obtained by anodizing. The researchers can prepare different nanotube morphologies by controlling key factors such as electrolyte composition, [104,105] applied voltage, [106] and oxidation time [107]. Zhang et al. [108] used graphite plates as counter electrodes, and immersed the titanium foil into electrolyte solution containing ethylene glycol, NH_4F, and ultrapure water. After being anodized and heated, TiO_2-NTs with an average inner diameter of about 46 ± 11 nm were obtained as conductive substrate (Fig. 4a). Next, graphite carbonitride (g-C_3N_4) and $Mn_3(BTC)_2$ was grown layer-by-layer on the TiO_2-NTs surface via liquid phase epitaxy method (Fig. 4b). Similarly, Jia and others finished the anodization with the electrolyte solution containing NaF and Na_2SO_4 [109]. In the subsequent treatment, they obtained pyramid TiO_2 by adding NH_4F powder into the muffle furnace to change the calcination atmosphere. Then ZIF-8/NF-TiO_2 photoelectrodes were prepared by in-situ growth for photo-electrocatalysis degradation of sulfamethazine (Fig. 4c).

However, the nanotubes obtained by anodized Ti foil generally have a lower Ti foil utilization rate, lower diffusion efficiency and conversion frequency due to the low permeability of the sheet material. Recently, Yang and his colleagues [101] proposed a strategy, they selected titanium metal mesh for anodization, and the 3D hollow-out TiO_2 nanowire cluster (NWc) obtained was more conducive to the exposure of the active site (Fig. 4d), the diffusion of the matrix and products. They divided the net into blocks, and anodized titanium mesh in an electrolyte composed of NH_4F, water, and ethylene glycol. The unique hollow nanocarbon structure of 3D hollow-out TiO_2-NWc increased the exposed area of the active site, and the network structure greatly improved the diffusion rate between the substrate and the solution (Fig. 4e).

In addition to the anodizing method, Jiao's team [110] developed another suitable TiO_2 matrix to host MOFs. Firstly, the team put the clean Ti foil and HCl into a stainless-steel autoclave lined with Teflon to prepare TiO_2. Subsequently, the Ti^{3+} doped TiO_2 sub-

Table 2
MOFs and their derivatives-modified photoelectrodes for PEC applications.

Series	Photoelectrode	PF of MOFs	Photo-electrocatalyst	IPCE	PEC application	Ref.
MIL	photoanode	MOFs	MIL-68(In)-NH_2/MWCNT/CdS	NA	Sensor	[111]
MIL	photoanode	MOFs	NH_2-MIL-125(Ti)/TiO_2	84.4%	Water splitting	[112]
MIL	photoanode	derivatives	M-TiO_2/CdSe@CdS	42.0%	Water splitting	[113]
MIL	photoanode	derivatives	$Ti_xFe_{1-x}O_y/Fe_2O_3$	47.0%	Water splitting	[114]
MIL	photoanode	MOFs	O-CNTs@MIL-88B(Fe)	NA	Sb (III) decontamination	[115]
MIL	photoanode	MOFs	MIL-100(Fe)/TiO_2	47.0%	Water splitting	[116]
MIL	photoanode	MOFs	MIL-101(Fe)/Mo: $BiVO_4$	46.8%	Water splitting	[72]
MIL	photoanode	MOFs	MIL-53(Fe)/Fe: $BiVO_4$	NA	Water splitting	[90]
MIL	photoanode	MOFs	Fe_2O_3: Ti/NH_2-MIL-101(Fe)	42.3%	Water splitting	[66]
MIL	photoanode	MOFs	Fe_2O_3/MIL-101(Fe)	26.6%	Water splitting	[117]
MIL	photoanode	MOFs	Fe_2O_3/MIL-53(Fe)	NA	PNP degradation	[12]
ZIF	photoanode	MOFs	Fe_2O_3@ZIF-67	23.3%	Water splitting	[81]
ZIF	photoanode	derivatives	ZnCdS@MoS_2	NA	Sensor	[118]
ZIF	photocathode	MOFs	C-Zn/Co-ZIF	NA	CO_2 reduction	[94]
ZIF	photoanode	MOFs	ZnO/N-CD@ZIF-8	7.2%	Water splitting	[97]
ZIF	photoanode	MOFs	ZIF-67/CNTs-g-C_3N_4/TiO_2	NA	Sensor	[119]
UiO	photoanode	MOFs	$[Ru(bpy)_3]^{2+}$@UiO-66	8.0%	Sensor	[120]
UiO	photoanode	MOFs	Au/UiO-66(NH_2)/CdS	NA	Sensor	[121]
PCN	photoanode	MOFs	C_{60}@PCN-224	NA	Sensor	[122]
PCN	photoanode	MOFs	PCN-224/rGO	NA	Sensor	[123]

[a] PF: participation forms.
[b] IPCE: incident-photon-to-electron conversion efficiency.
[c] PNP: p-nitrophenol.
[d] NA: Not available.

strate was obtained after TiO_2 being placed again in stainless-steel autoclave lined with Teflon containing N_2H_4 aqueous solution. The presence of Ti^{3+} increased the surface defects and enhanced the interaction between the ligand in the MOF precursor solution and the TiO_2 surface, which was beneficial to the subsequent one-pot synthesis method for heteroatom doping and oxide surface modification. Applying the above strategies, they successfully obtained In-Ni/N/TiO_2 photoelectrode.

4. Common MOFs series in photoelectrodes

MOFs commonly used in PEC applications include MIL series, ZIFs series, UiO series, and PCN series. In addition, derivatives of MOFs have also been reported to be used in PEC systems due to their significantly improved photo-electrochemical performance (Table 2). In the following section, the performance and mechanism of these MOFs and their derivatives in PEC applications will be discussed in detail.

4.1. MIL-modified PEC photoelectrodes

The study of MOFs-modified PEC photoelectrodes is still in the preliminary stage, and the research basis is relatively weak. Among various MOFs series, the research work of MIL series of MOFs-based photoelectrodes is relatively rich and mature. MIL is mostly synthesized by the interaction of iron, aluminum, chromium and other metal ions with organic ligands [124]. And common MIL-modified PEC photoelectrodes include indium-based MOFs, titanium-based, and iron-based.

4.1.1. Indium-based MOFs

At present, the research on indium-based MOFs modified photoelectrodes for photo-electrocatalysis is very limited. For example, Zhang's team [111] studied indium-based MOFs photoelectrodes by in-situ deposition. The transmission electron microscopy (TEM) image showed that pure CdS was aggregated nanospheres (Fig. 5a). After adding MIL-68(In)-NH_2/MWCNT, the growth and aggregation of CdS nanoparticles could be effectively inhibited (Fig. 5b). It could be seen from the HRTEM image (Fig. 5c) that CdS nanoparticles form a tight contact with MIL-68 (In)-NH_2, and together with the functionalized MWCNTs, adjusted the electron transport path and further promoted the transfer and separation of carriers. The obtained MIL-68(In)-NH_2/MWCNT/CdS composite electrode could react with tetracycline (TC) molecules to form a PEC sensor through specific interaction, and the fluctuation of the photocurrent signal successfully respond to the concentration range of 0.1 nmol·L^{-1} to 1 μmol·L^{-1} TC content.

4.1.2. Titanium-based MOFs

Due to the abundant optical research foundation of TiO_2, titanium-based MOFs are also being considered for the construction of photoelectrodes. In the research of photoelectrodes, the common Ti-based MOFs is MIL-125 (Ti), which is composed of quasi-cubic tetragonal system and octameric $Ti_8O_8(OH)_4$ oxo clusters connected with amino-dicarboxylate linkers. The key features are high porosity, presence of tetragonal (6.1 Å) or octahedral cavity (12.5 Å), accessible micropores (5–7 Å), and good chemical stability in organic solvents. Sharma et al. [99] reported that a composite electrode of MIL-125 (Ti) and single-walled carbon nanotubes (CNT) was used as the active photoelectric layer in dye-sensitized solar cells (DSSC). The CNTs provided excellent electrical conductivity, and MIL-125 (Ti) enhanced the light absorption capacity and used the porous nature to minimize charge recombination. Finally, the power conversion efficiency of MIL-125/SWCNT DSSC increased from 2.68% of MIL-125(Ti) to 5.26%. NH_2-MIL-125 (Ti) is an excellent photocatalyst with 2.6 eV band gap, and its titanium oxide cluster is coordinated with an organic linker (i.e. 2-aminoterephthalic acid) [125]. It exhibits higher water stability than MIL-125(Ti), enabling semiconductor applications under visible light. Yoon et al. [112] designed the structure of the TiO_2 nanorods coated with the photosensitive NH_2-MIL-125(Ti) to study the performance of MOF/semiconductor heterojunction photoelectrode in PEC water splitting. The (II) band arrangement (Fig. 5d) was beneficial to the electrons transfer from the conduction band (CB) of NH_2-MIL-125(Ti) to the CB of TiO_2. Under the light of AM 1.5G, the photocurrent density of NH_2-MIL-125(Ti)/TiO_2 could reach to 1.63 mA·cm^{-2} at 1.23 V vs RHE, which was 2.7 times that of the original TiO_2 nanocrystals.

In addition to directly forming heterojunctions with semiconductors, MOFs can also combine with semiconductors in the form

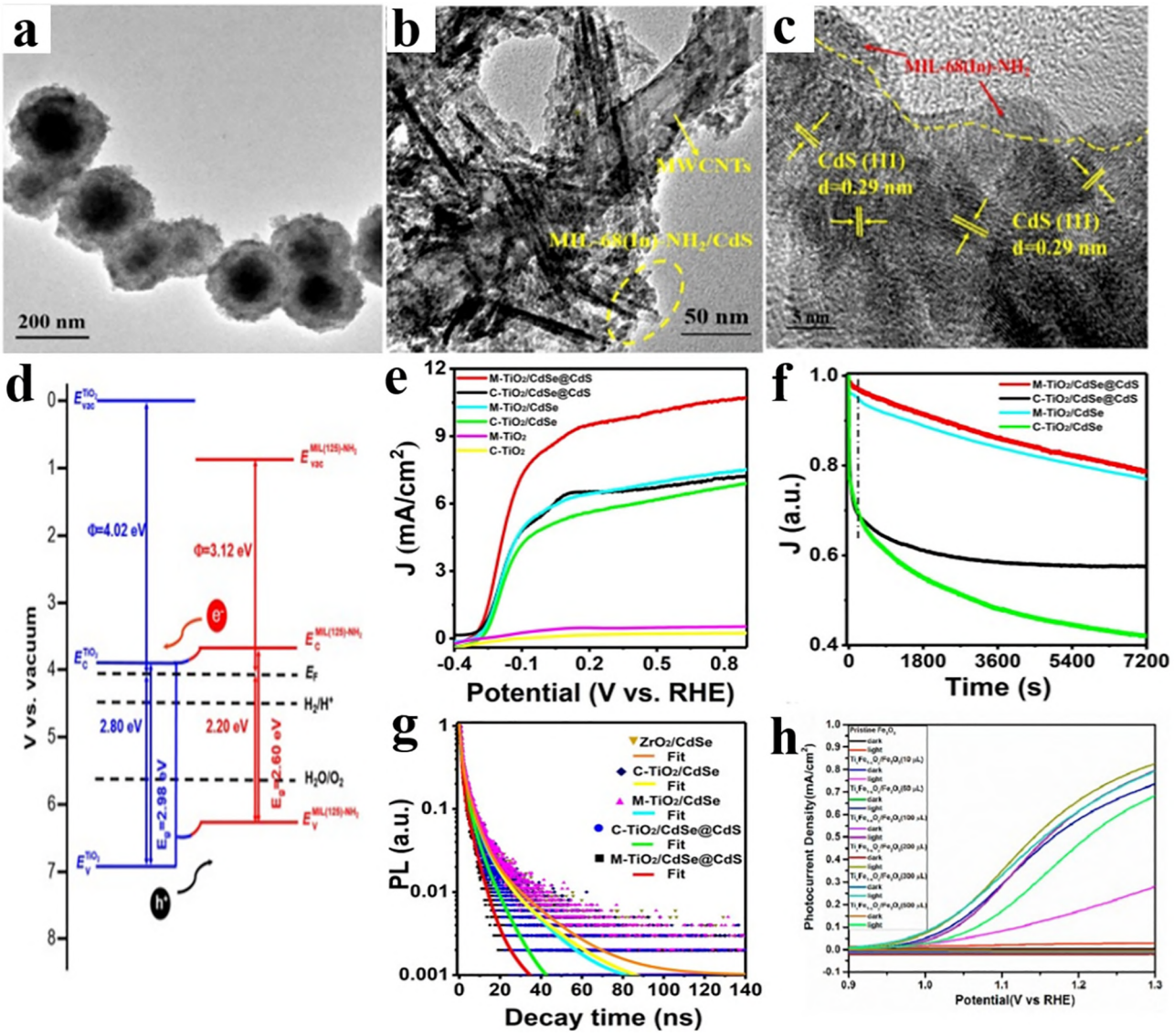

Fig. 5. (a) TEM images of CdS and (b) MIL-68(In)-NH_2/MWCNT/CdS. HRTEM image of (c) MIL-68(In)-NH_2/MWCNT/CdS. (a-c) are reproduced with permission from Ref. [111]. Copyright 2019 Elsevier. (d) Schematic energy band diagram of the MIL (125)-NH_2/TiO_2 NR heterojunction photoanode. Reproduced with permission from Ref. [112]. Copyright 2019 Elsevier. (e) Photocurrent density potential dependence of M-TiO_2 and C-TiO_2 sensitized by CdSe and CdSe@CdS. (f) Stability measurements (photocurrent density as a function of time) of M-TiO_2 and C-TiO_2 sensitized by CdSe and CdSe@CdS photoanodes at 0.4 V versus RHE under AM 1.5 G illumination (100 mW·cm^{-2}). (g) Transient PL spectra of ZrO_2/CdSe, C-TiO_2/CdSe, M-TiO_2/CdSe, C-TiO_2/CdSe@CdS and M-TiO_2/CdSe@CdS. (e-g) are reproduced with permission from Ref. [113]. Copyright 2020 Elsevier. (h) Photo-current density vs. applied potential curves for $Ti_xFe_{1-x}O_y/Fe_2O_3$ electrodes fabricated at six different Ti precursor additions and pristine Fe_2O_3 nanorod array electrode. Reproduced with permission from Ref. [114]. Copyright 2019 Elsevier.

of derivatives to exert more advantages. Shi et al. [113] explored the work of colloidal quantum dots sensitizing MOFs-derived TiO_2. Specifically, they used NH_2-MIL-125(Ti) as sacrificial template to synthesize anatase–rutile mixed-phase TiO_2, and used core–shell CdSe@CdS quantum dots to sensitize TiO_2, thereby obtaining M-TiO_2/CdSe@CdS. With the existence of a mixed phase TiO_2, the spatial separation of e^- and h^+ increased, further reducing recombination effects. The favorable electronic band alignment of the M-TiO_2/QDs could extract a large number of e^- and h^+ from QDs into M-TiO_2, thereby contributing to the improvement of current density. At 0.9 V vs RHE, the saturation photocurrent density of M-TiO_2/CdSe@CdS reached to 10.72 mA·cm^{-2}, which increased more than 47.6% than industrial pure anatase TiO_2 C-TiO_2/CdSe@CdS (7.24 mA·cm^{-2}) (Fig. 5e). Meanwhile, the shell-core structure effectively isolated the core material from the QDs surface chemistry and the surrounding chemical environment, thereby reducing surface defects and improving the PEC stability [126] (Fig. 5f). The tunable band gap and good energy band arrangement of quantum dots, and the formation of controlled mixed phases (anatase and rutile) were conducive to good electron band orientation and fast charge transfer (Fig. 5g). Li et al. [114] also did an excellent job in titanium-based MOFs derivatives. They heat-treated in situ NH_2-MIL-125(Ti) to form $Ti_xFe_{1-x}O_y/Fe_2O_3$ shell-core photoelectrode. When calcined at high temperature, uniform and ordered Ti ions in MOF enter Fe_2O_3 to replace part of Fe ions. The resulting structural defects could be used as photogenerated holes trapping points, and promoted carrier separation. The PEC performance of the composite electrode was significantly higher than that of the original Fe_2O_3 electrode, under simulated illumination AM 1.5 G, the photocurrent density was

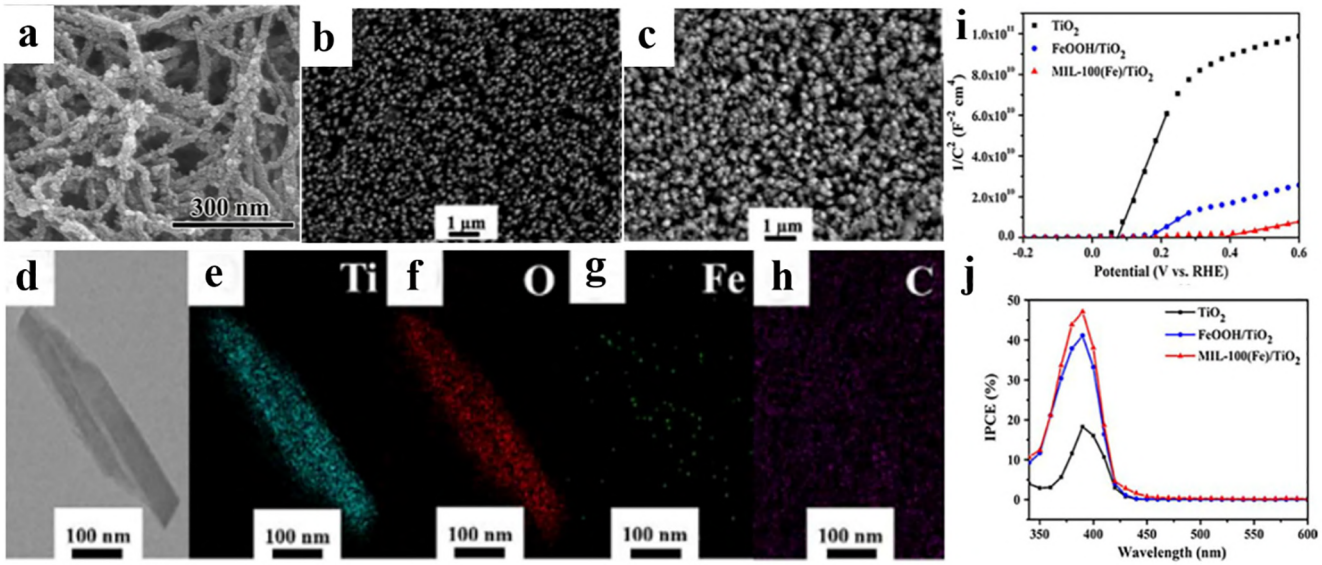

Fig. 6. (a) SEM images of as-prepared CM hybrids. Reproduced with permission from Ref. [115]. Copyright 2020 Elsevier. SEM images for (b) TiO_2 and (c) MIL-100(Fe)/TiO_2. (d-h) Corresponding EDS elemental mappings for MIL-100(Fe)/TiO_2. (i) Mott-Schottky plots at a specific frequency of 1 kHz. (j) IPCE spectra of TiO_2, FeOOH/TiO_2 and MOI-100 (Fe)/TiO_2. (b-j) are reproduced with permission from Ref. [116]. Copyright 2019 Wiley.

26.7 times that of Fe_2O_3 nanorod array electrode (at 1.23 V vs. RHE) (Fig. 5h).

4.1.3. Iron-based MOFs

Indium-based MOFs and titanium-based MOFs have played a role in PEC applications, while iron-based MOFs have more application advantages due to their low cost-effectiveness, wide distribution range, high soil abundance and non-toxicity [127]. For example, Li et al. [115] developed a PEC filter composed of CNTs and iron-based MOF (MIL-88B(Fe)). The highly toxic Sb (III) was simultaneously oxidized and adsorbed by Fe-based MOF, which exhibited high affinity for Sb (V). As shown in the Fig. 6a, MIL-88B(Fe) NPs were uniformly coated on the sidewalls of CNTs. CNTs were used as conductive supports, and MIL-88B(Fe) was used as an adsorbent and catalyst. The resulting hybrid filter has high specific surface area and abundant carriers. Under the optimal synthesis conditions, the Sb (III) transformation rate of the three-dimensional network structure could reach 97.7 ± 1.5%, and the total removal rate of Sb (III) was 92.9 ± 2.3%. However, it must be mentioned that due to the compatibility of the matrix, the formation of the heterogeneous interface was always accompanied by the introduction of defects, which reduced the carrier density in some extent.

In response to this problem, Cui et al. [116] successfully modified MIL-100(Fe) prepared by the FeOOH sacrificial template method on TiO_2 for PEC water oxidation, and the dense ultra-thin MIL-100(Fe) film was tightly anchored on vertically oriented TiO_2 nanorods surface. The Scanning electron microscopy (SEM) image showed that the morphology of MIL-100(Fe)/TiO_2 was almost the same as that of TiO_2 (Fig. 6b-c), which indirectly indicated that MIL-100(Fe) existed in the form of ultrathin film. The Energy-dispersive X-ray spectroscopy (EDS) (Fig. 6d-h) element mapping more intuitively showed the uniform distribution of Fe and C elements around TiO_2 nanorods. When MIL-100(Fe) was modified on the TiO_2 surface, rich unsaturated Fe-site active centers rapidly consumed the captured photogenerated holes, and maintained a high carrier density. This could be confirmed from the Fig. 6i, MIL-100(Fe)/TiO_2 not only had a distinct positive shift of flat band potential, but also had the gentlest slope. The in-situ modification could produce strong graft bonds between heterogeneous interfaces, effectively suppressing interface defects and reducing carrier recombination. While the red shift of the IPCE curve of MIL-100 (Fe)/TiO_2 was not obvious (Fig. 6j), implying that the ultra-thin film of the MIL-100(Fe) matrix bright new problems of limited light absorption.

Liu et al. [72] utilized MIL-101(Fe) with good visible light response as the shell layer and coated it on the Mo-doped $BiVO_4$ surface to obtain MIL-101(Fe)/Mo: $BiVO_4$ photoanode with high light absorption capacity and high PEC activity. Due to the good visible light response of MIL-101(Fe) shell layer, the photocurrent density for the MIL-101(Fe)/$BiVO_4$ increased from 1.53 mA·cm^{-2} of $BiVO_4$ to 2.59 mA·cm^{-2}. Under the synergistic effects of Mo-doping and MIL-101 (Fe) coating, the photocurrent density of MIL-101(Fe)/Mo: $BiVO_4$ continued to increase to 4.01 mA·cm^{-2}, which was 1.55, 2.52, and 3.64 times higher than that of MIL-101 (Fe)/$BiVO_4$, Mo: $BiVO_4$, and $BiVO_4$ photoanodes, respectively (Fig. 7a). In addition, the surface injection efficiency and charge separation efficiency of MIL-101(Fe)/Mo: $BiVO_4$ were significantly improved (Fig. 7b-c), and the separation efficiency was improved to a greater extent than the injection efficiency, further indicating that Mo doping and MOF coating promoted holes enter the water through the electrode/electrolyte interface more quickly and were utilized in time. Similar work has been carried out for efficient water oxidation (Fig. 7d) [90]. The difference was that Fe was doped into $BiVO_4$ to improve the stability of $BiVO_4$ and thus maintaining the photocurrent of photoelectrode at a constant value (Fig. 7e). During the doping process, iron ions replaced few of Bi ions, improving the crystal structure of $BiVO_4$ and eliminating crystal defects. Fe doping was not only beneficial to the stability and light conversion efficiency, but also could cooperate with the co-catalyst (MIL-53(Fe)) to further improve the light absorption capacity and carrier separation efficiency (Fig. 7f).

The above work has confirmed that the formation of ultra-thin films was conducive to ameliorate the performance of PEC, but the quality of the film was not always satisfactory. Therefore, fine control of the MOFs coating was the key to achieving high PEC performance. Dong et al. [66] used surfactant to controllably construct a semiconductor/MOFs core/shell heterostructure for PEC water splitting. They selected PVP molecules as mediators to controllably grow ultra-thin MOF shells of a few nanometers thick on the sur-

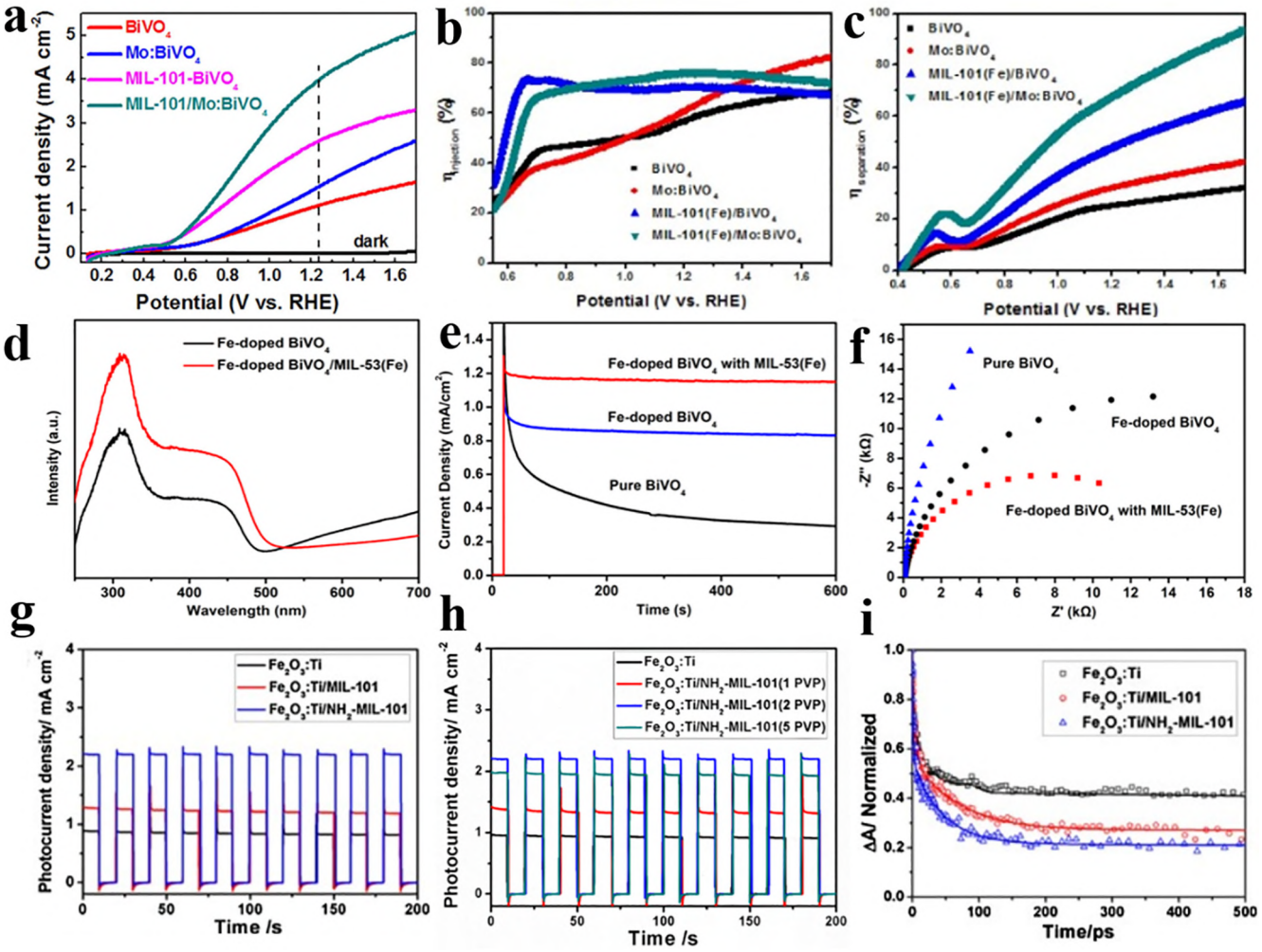

Fig. 7. (a) LSV curves of pristine $BiVO_4$, MIL-101(Fe)/$BiVO_4$, Mo: $BiVO_4$ and MIL-101(Fe)/Mo: $BiVO_4$ photoanodes. (b) and (c) the injection and separation efficiency for the $BiVO_4$ photoanodes. (a-c) are reproduced with permission from Ref. [72]. Copyright 2020 Elsevier. (d) UV/Vis absorption spectra of Fe-doped $BiVO_4$ with and without MIL-53 (Fe). (e) Current-time stability test and (f) Nyquist plots of the electrochemical impedance spectra of Fe-doped $BiVO_4$ with and without MIL-53(Fe). (d-f) are reproduced with permission from Ref.[90]. Copyright 2019 Springer. (g) without PVP and (h) with PVP at 1.23 V vs. RHE, under chopped under AM 1.5G simulated sunlight of 100 $mW{\cdot}cm^{-2}$. (i) Transient absorption decay curves at 570 nm of different photoanodes upon 355 nm (200 $\mu J{\cdot}cm^{-2}$, 1000 Hz). (g-i) are reproduced with permission from Ref. [66]. Copyright 2018 Elsevier.

face of Fe_2O_3 nanorods. Although the samples prepared without PVP also exhibited enhanced visible light absorption (Fig. 7g), the photocurrent shown by the composite electrode was similar to the Fe_2O_3: Ti electrode, which indicated that the Fe_2O_3 nanorods might have poor contact with the MOF nanoparticles. Notably, when the thickness of the film increased, the conductivity would decrease. (Fig. 7h). In addition, the author used ultrafast transient absorption spectroscopy to report the dynamics of photogenerated carriers (Fig. 7i). The Fe_2O_3: Ti/MOF sample showed the fastest decay on the picosecond time scale, with lifetime $\tau_{1/2}$ of 7.43 ps for Fe_2O_3: Ti/NH_2-MIL-101(Fe) and 17.8 ps for Fe_2O_3: Ti/MIL-101 (Fe). The rapid attenuation of the absorption signal meant that holes were extracted by the MOF shell in time, and thus avoiding being trapped by surface traps, which was beneficial to the separation of charge and the suppression of electron/hole recombination. Similarly, Wang et al. [117] adjusted the photoelectric response capability of the film by controlling the thickness of the MIL-101 layer. In order to avoid the problems of rapid nucleation and agglomeration in the traditional solvent process, Wang et al. improved to the construction method of heterojunctions. They used chemical vapor deposition to prepare Fe_2O_3/Fe-MOF nano-hetero junction, and explored the influence of deposition time on the PEC performance. As we can see from the Fig. 8a, the continuous dense film of Fe_2O_3/MIL-101(Fe) was successfully formed. The morphological identification results of TEM (Fig. 8b) showed that there was no obvious interface boundary between Fe_2O_3 NAs and MIL-101(Fe) layer. The dense interfacial contact was be conductive to the rapid carrier transmission between Fe_2O_3 and MOF. Meanwhile, the effective suppression of carrier recombination was confirmed by linear voltammetry scan (LSV) results (Fig. 8c), and the initial potential of Fe_2O_3/MIL-101(Fe) was significantly negatively shifted, which further proved more holes to participate in surface water oxidation reaction.

Currently, the research on the construction of MOFs photoelectrodes for PEC application is relatively limited. Most of the research is mainly focused on the water oxidation, and the function of photoelectrode is relatively single. Zhang et al. [12] prepared a multifunctional MOF-modified photoelectrode, which was composed of magnetic Fe_3O_4 nanospheres decorated with MIL-53(Fe) microrods. As shown in Fig. 8d and e, Fe_3O_4 nanospheres were dispersedly anchored to the MIL-53(Fe) microrods surface. After adding Fe_2O_3, multifunctional hybrid magnetic composites (MHMCs) had excellent magnetic sensitivity. And it exhibited near-zero coercive force and remanence at room temperature, the saturation magne-

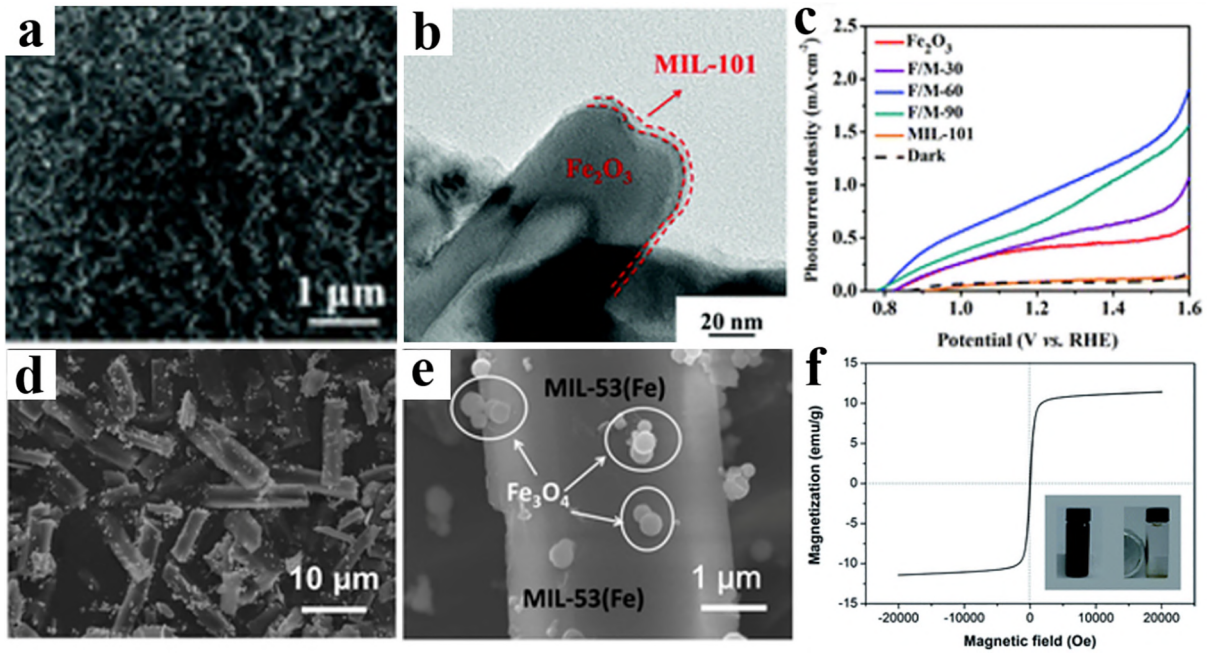

Fig. 8. (a) SEM images of the F/M-60. (b) The magnified TEM image of the F/M-60. (c) LSV curves of Fe_2O_3, MIL-101 and Fe_2O_3/MIL-101 photoanodes. (a-c) are reproduced with permission from Ref. [117]. Copyright 2019 RSC. (d) and (e) SEM images of MHMCs. (f) Magnetization hysteresis curve of the MHMCs. (e-f) are reproduced with permission from Ref. [12]. Copyright 2014 The Royal Society of Chemistry.

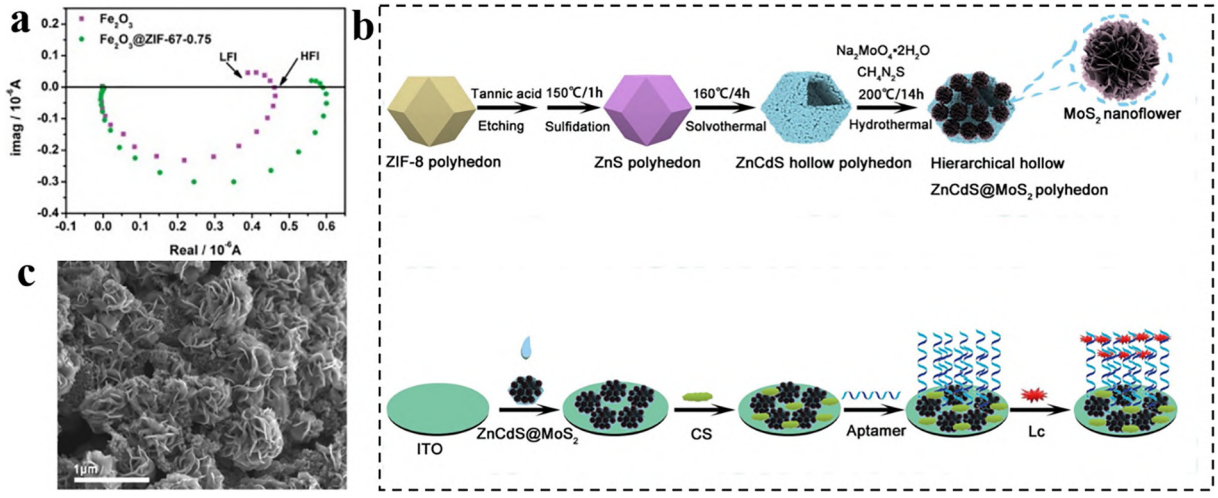

Fig. 9. (a) IMPS plot of Fe_2O_3 and Fe_2O_3@ZIF-67 photoanodes. Reproduced with permission from Ref. [81]. Copyright 2020 Elsevier. (b) Schematic illustration of fabrication of hierarchical hollow ZnCdS@MoS_2 hetero-structured cages. (c) ZnCdS@MoS_2 hetero-structured cages. (b-c) are reproduced with permission from Ref. [118]. Copyright 2020 Elsevier.

tization of MHMCs could reach 11.47 emu·g^{-1} (Fig. 8f). Under visible light irradiation, MIL-53(Fe) could be excited and generate photocurrent via the d-d transition spin-allowed by the iron-oxo cluster of Fe^{3+}. The formed MHMCs film could be used as a photoelectrode to promote PEC water oxidation, and used as a photocatalyst in the visible light catalysis process mediated by H_2O_2.

4.2. ZIF-modified PEC photoelectrodes

ZIF are a subclass of MOFs with the same topologies and water stability as aluminosilicate zeolites [128]. In addition to N^- moieties and OH groups, unsaturated cations (acidic centers) located on the external surface are served as the basic active centers of ZIFs [129]. The synthesis conditions of ZIFs are relatively mild, and can be synthesized even at room temperature. Therefore, ZIFs are not be limited by the synthesis conditions in the construction of PEC devices, and they also perform well in the construction of PEC devices. In the latest research, Li et al. [81] completed the work of growing ZIFs coating on semiconductors. Due to the high-efficiency electrocatalytic water oxidation activity of ZIF-67 in alkaline electrolyte system, Li and his colleagues grew ZIF-67 on α-Fe_2O_3 nano array for PEC water splitting via a simple surface-assisted controlled synthesis method. The abundant cobalt and 2-methylimidazole ligands of ZIF-67 acting as redox mediators and proton transfer centers, could lead to charge separation capacity. The results of the intensity modulation photocurrent spectroscopy (IMPS) (Fig. 9a) on the charge transport characteristics displayed that the introduction of ZIF-67 increased the hole-to-surface flux,

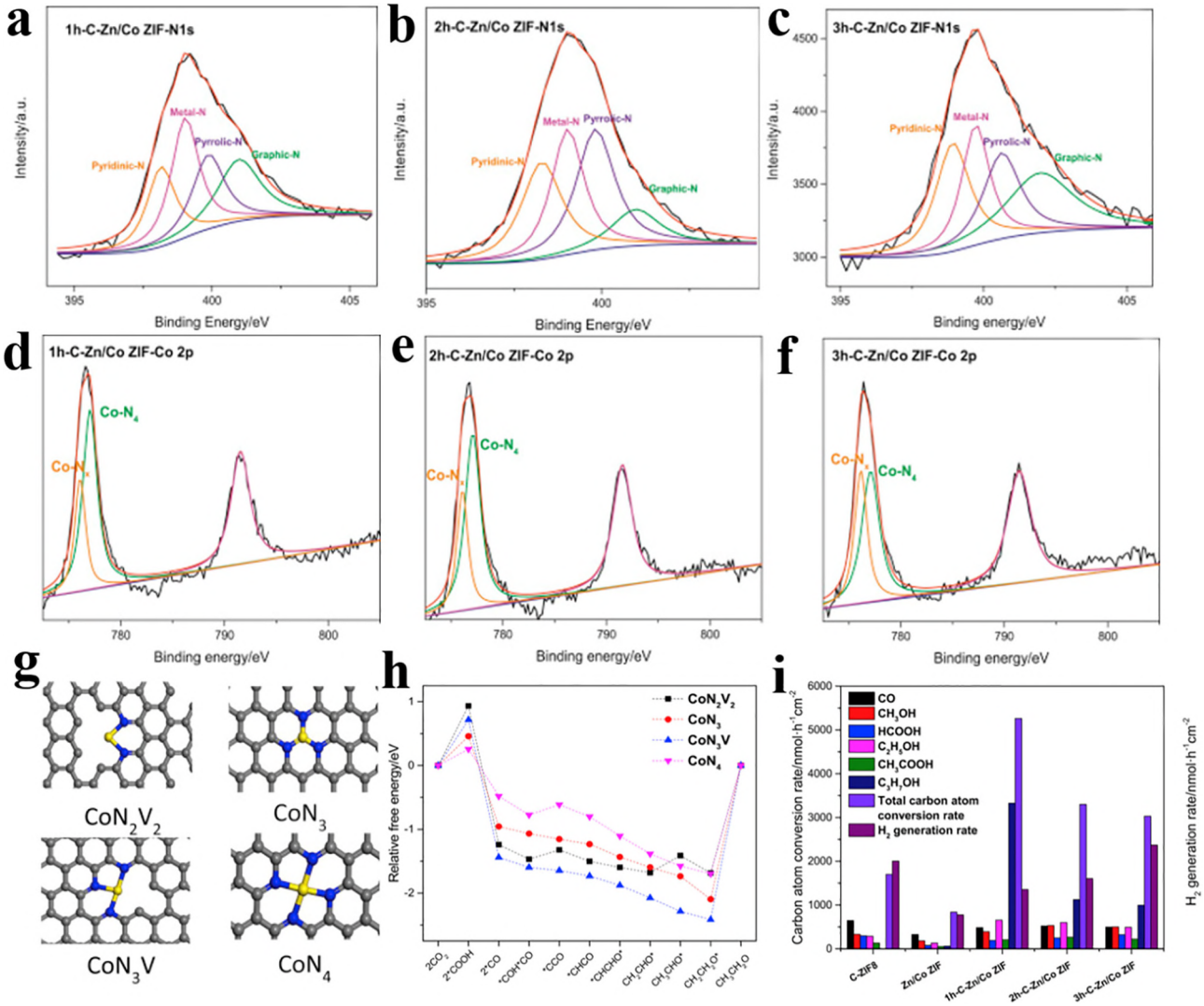

Fig. 10. N 1s XPS spectra of (a) 1 h-C-Zn/Co ZIF, (b) 2 h-C-Zn/Co ZIF and (c) 3 h-C-Zn/Co ZIF. Co 2p XPS spectra of (d) 1 h-C-Zn/Co ZIF, (e) 2 h-C-Zn/Co ZIF and (f) 3 h-C-Zn/Co ZIF. (g) Four possible geometries of the Co-N sites (grey atom: carbon atom, blue atom: nitrogen atom, yellow atom: cobalt atom). (h) Free energy pathways of ethanol producing process on four possible Co-N sites. (i) Carbon atom conversion rate and H_2 generation rate with various catalysts applied of CO_2 photoelectrochemical reduction over various catalysts of Zn/Co ZIF and C-Zn/Co ZIF catalysts. (a-i) are reproduced with permission from Ref. [94]. Copyright 2019 Elsevier.

thereby reducing the surface charge recombination, and accelerated water oxidation reaction kinetics.

Apart from being grown on the semiconductor surface and used directly in the construction of PEC devices, ZIFs also excel in the preparation of functional materials with specific morphologies as precursors. For example, Zhang et al. [118] first constructed a C@ZnCdS polyhedron cage by the simple sintering method. To further promote the separation of photogenerated carriers, ZnCdS@MoS_2 heterostructure cage was constructed to obtain a more intimate contact between the heterojunction interface (Fig. 9b). The new heterostructure cage exhibited higher charge separation efficiency through the customized morphology and intimate contact between the heterojunction interface. And the simultaneously formed multi-layer hollow heterostructure (Fig. 9c) could promote more photo-harvesting by multilight scattering/reflection, and thus improving the ability to capture visible light. Meanwhile, the aggregation of MoS_2 was also greatly weakened by the layered hollow heterostructure. Finally, compared with ZnCdS and MoS_2, the PEC response of ZnCdS@MoS_2 was improved by 3.1 times and 47.3 times, respectively. And the detection limit of the obtained PEC sensor for Lincomycin was 7.6×10^{-11} mol·L^{-1} and the linear response range was 1×10^{-10}–3×10^{-7} mol·L^{-1}.

Considered that higher charge transfer capacity and adsorption capacity of the carbon-based catalyst obtained after pyrolysis, Cheng et al. [94] also had done research on ZIF-derivatives. The team directly pyrolyzed Zn/Co-ZIF, which could act the source of nitrogen-carbon. They used N doping to change the electronic and geometric properties of the catalyst, and simultaneously studied the catalytic effect of Co-N sites. X-ray photoelectron spectroscopy (XPS) results showed that the proportion of metal-N in 1h-C-Zn/Co-ZIF, 2h-C-Zn/Co-ZIF and 3h-C-Zn/Co-ZIF compounds decreased (Fig. 10a-c), while the proportion of Co species increased (Fig. 10d-f). In line with the Co-N coordination principle, the team defined several possible Co-N_x (x > 4) geometries (Fig. 10g). To study the CO_2 photoelectrochemical reduction reaction (CO_2 PRR) and its catalytic activity on possible structures, they calculated the free energy of intermediates involved in producing ethanol reaction pathways on each Co-N_x geometry. In general, the free energy of the intermediate product G*COH*CO can best reflect the selectivity of CO_2 PRR to higher-order liquid fuels. According to the Density functional theory (DFT) calculation results (Fig. 10h and i), CoN_3V had the lowest free energy at G*COH*CO, indicating that the unsaturated CoN_3V site in C-Zn/Co-ZIF had the most excellent catalytic activity. Correspondingly, the CO_2

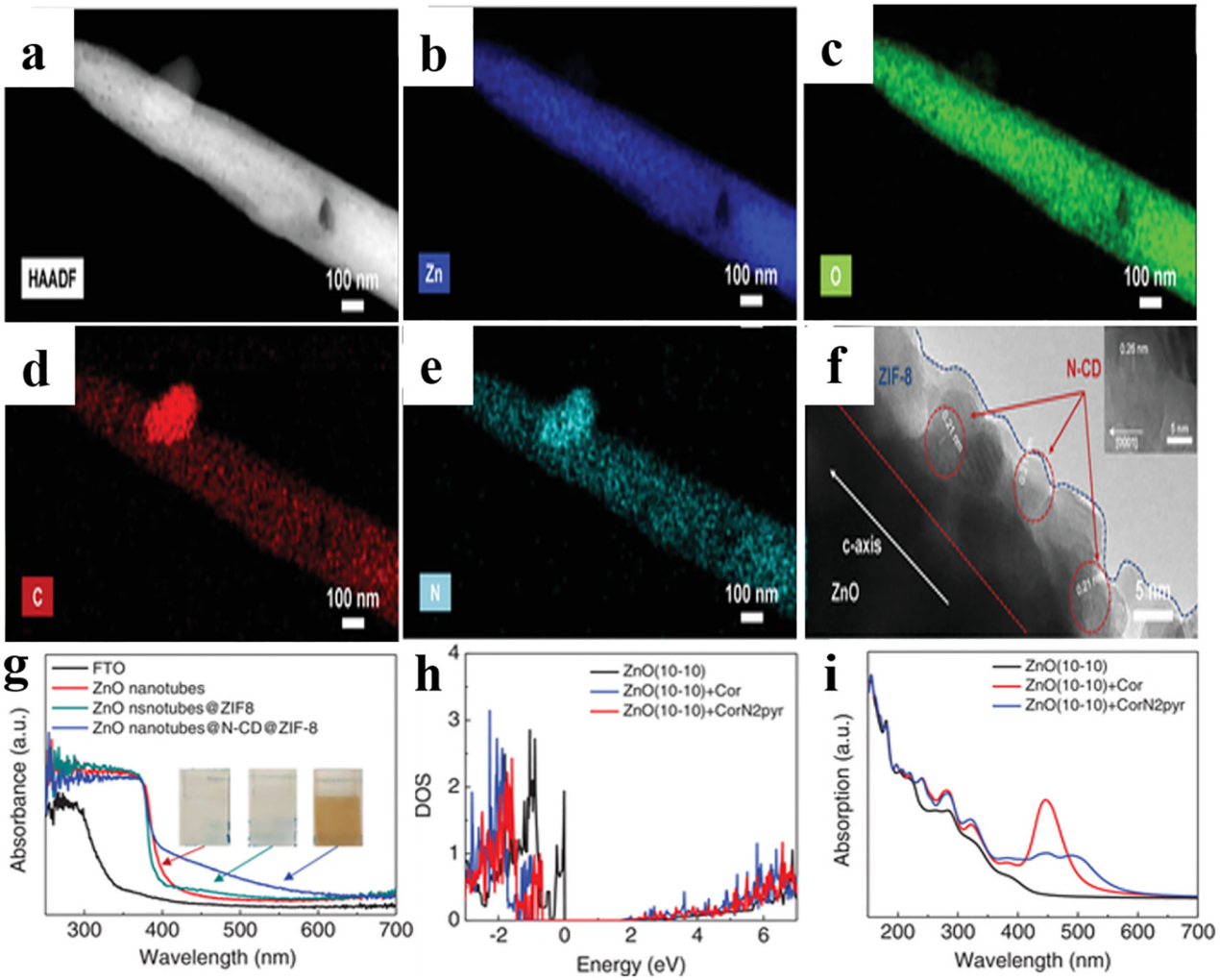

Fig. 11. (a-e) HAADF images and (f) HRTEM image of ZnO nanotubes with N-CD embedded ZIF-8. (g) UV–vis absorption spectra of ZnO nanotubes, ZnO nanotubes with ZIF-8, and ZnO nanotubes with N-CD embedded ZIF-8. (h) Density of electronic states and (i) optical absorption spectra for ZnO (10–10) surface, ZnO (10–10) with adsorbed coronene (Cor), and ZnO (10–10) with adsorbed N-coronene. (a-i) are reproduced with permission from Ref. [97]. Copyright 2019 Wiley.

PRR experiment showed the 1h-C-Zn/Co-ZIF catalyst had the highest selectivity for high-order liquid fuels (Fig. 10j), and the total carbon atom conversion rate reached to 5459 nmol·cm^{-2}h^{-1}. Combining XPS and CO_2 PRR experimental results, the author believed that 1h-C-Zn/Co-ZIF catalyst contained most CoN_3V sites. The above characteristics of the catalyst are conducive to the binding of intermediate products on the surface, making it easier to produce higher-order products.

Han and his colleagues [97] had also done research on N doping. Interestingly, this was a work on nitrogen-doped carbon dots (N-CDs). They used ZIF-8-derivative ZnO as the host and N-CDs as the guest. The obtained photoelectrode exhibited enhanced light absorption and improved photocurrent density. TEM images and corresponding EDX showed that ZIF-8 and N-CDs were homogeneously distributed on ZnO surface (Fig. 11a–f). The N-CD embedded ZIF-8 on ZnO-NTs not only provided facile electron pathway because of their ordered structure (Fig. 11g), but also increased the light harvest range and promoted the separation of e^-/h^+ pairs. The author further examined the light absorption capacity through DFT calculation (Fig. 11h and i). The density of electronic states indicated that when coronene or N-doped coronene (CorN2pyr) were added to ZnO, the band gap value was reduced: 2.93 eV for ZnO, 1.96 eV for ZnO + CorN2pyr, confirming that N-CDs would change Fermi energy level arrangement to form red shift.

The above work on ZIFs had focused on the research of a single photoelectrode, while Dou et al. [119] had grown ZIF-67 and ZIF-8 on the CNTs-g-C_3N_4/TiO_2-NTs, respectively. And they constructed the PEC-H_2O_2 sensor with the obtained photoelectrode. The same pore size of ZIF-67 and ZIF-8 could effectively avoid the diffusion of substances in the coating and allow the diffusion of H_2O_2 molecules, and thus obtaining a coating with catalytic effect and molecule filtering effect. Since ZIF-67 has good catalytic effect on H_2O_2, and ZIF-8 has no catalytic effect on H_2O_2, ZIF-67/CNTs-g-C_3N_4/TiO_2-NTs was used as a sensitive photoelectrode, while ZIF-8/CNTs-g-C_3N_4/TiO_2-NTs was used as the reference photoelectrode. The sensitivity of the sensing photoelectrode to H_2O_2 was higher than that of the reference photoelectrode, and the difference strategy was used to effectively eliminate the interference of the larger size molecules on the photoelectrode surface. Finally, a high sensitivity and anti-interference ability PEC sensor was obtained with 1.5 nmol L^{-1} detection limit for H_2O_2.

4.3. UiO-modified PEC photoelectrodes

Up to now, the MILs-modified PEC photoelectrodes and ZIFs-modified PEC photoelectrodes have excellent performance in water oxidation, CO_2 reduction, etc. Compared with the first two, the UiO series with good biocompatibility has also achieved new progress

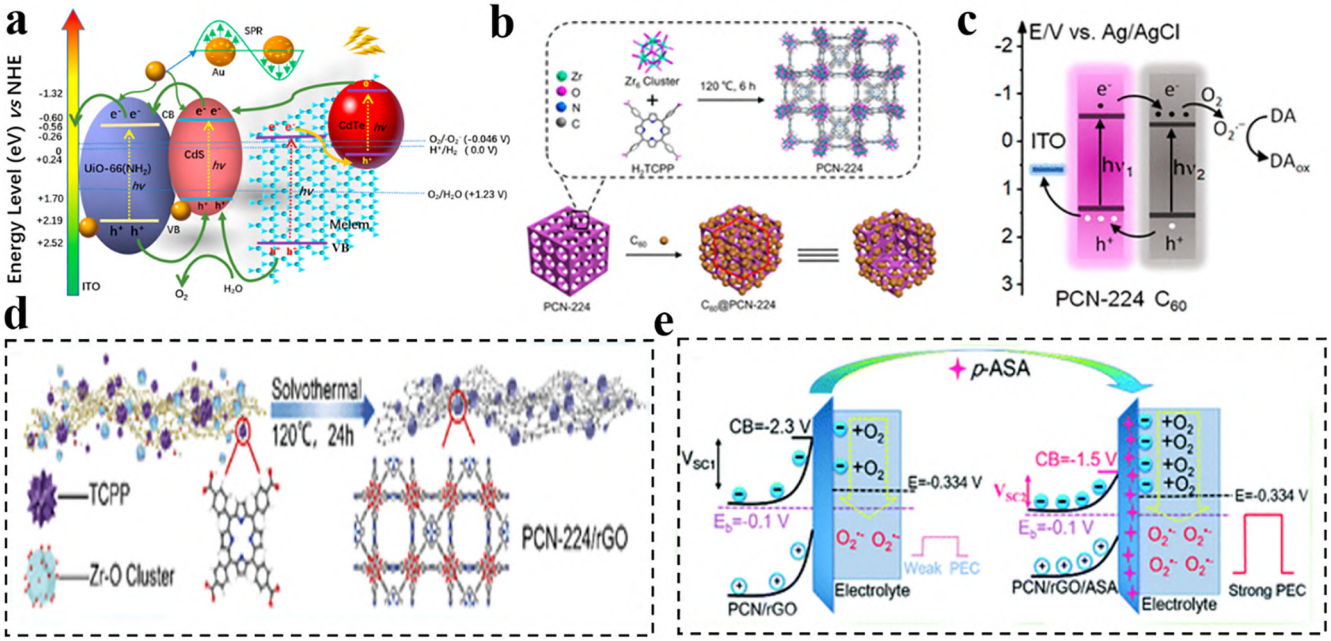

Fig. 12. (a) The electron-transfer mechanism of the PEC immunosensor. Reproduced with permission from Ref. [121]. Copyright 2018 Elsevier. (b) Brief procedure for C60@PCN-224 assembly. (c) Proposed charge transfer mechanism of photocurrent generation of C60@PCN-224. (b-c) are reproduced with permission from Ref. [122]. Copyright 2020 American Chemical Society. (d) The design illustration of preparing PCN-224/rGO nanocomposite. (e) Illustration of the mechanism of photocurrent enhancement through adsorption of p-ASA on the PCN/rGO electrode. (d-e) are reproduced with permission from Ref. [123]. Copyright 2019 The Royal Society of Chemistry.

in PEC biosensors. UiO is an important branch of MOFs and they are synthesized with metal zirconium ions as the metal center [130]. This series of MOFs materials have broken through the limitations of relatively small pore sizes like zeolites. Take UiO-66 as an example, it is composed of $[Zr_6O_4(OH)_4]$ cluster compound and 1,4-phthalic acid, has chemical stability, non-toxicity and good biocompatibility, and has high porosity to accommodate a variety of photosensitive molecules [131]. Inspired by known oxides with strong affinity for phosphate groups, Wang et al. [120] made the assumption that the $[Zr_6O_4(OH)_4]$ cluster in UiO-66 might have strong binding ability to phosphate groups. In order to verify the idea, they first prepared a phosphorylated kemptide-modified TiO_2/ITO electrode, and combined with UiO-66, which pores was introduced $[Ru(bpy)_3]^{2+}$. Finally, a PEC biosensor for the detection of ultrasensitive protein kinase A activity determination was successfully obtained. This report confirmed the high affinity of the Zr-O clusters for phosphate groups, and the Zr-O-P bonds could be used as anchorages to identify phosphate groups. Therefore, the high affinity for phosphate groups made UiO more useful for the enrichment of phosphates and phosphonates. Subsequently, Wu et al. [121] also used UiO-66 as the anchorage of phosphate group, and designed a novel PEC sensor via using multiple photocurrent signal amplification technology. They reduced Au NPs in situ and modified the CdS NPs on the UiO-66(NH_2) substrate, thereby preparing a new PEC sensor-Au/UiO-66(NH_2)/CdS for diethylstilbestrol detection. During the detection process, the concentration of diethylstilbestrol could be directly reflected by the photocurrent. As shown in Fig. 12a, the photogenerated e^- in the CB of CdS could be injected into the CB of UiO-66(NH_2), and further transferred to the ITO electrode. Au NPs could inject hot electrons into the CB of CdS and UiO-66(NH_2) while accelerating electron transfer. Similarly, the e- in CdTe would be quickly injected into CdS due to the matching energy levels. The holes (h^+) generated in Melem and UiO-66(NH_2) would be transferred to the VB of CdS and react with H_2O to generate O_2. The designed PEC immunosensor linear range was from 0.1 pg·mL^{-1} to 20 ng·mL^{-1}, and the detection limit was 0.06 pg·mL^{-1}.

4.4. PCN-modified PEC photoelectrodes

The PCN are composed of multiple cubic octahedral cages and forms a cage-channel topology in space [132]. Due to the excellent photoelectric activity and environmental stability, the research on the application of PCN series materials in photoelectrodes focuses on PCN-224. It is a porphyrin MOF with carboxyl-group terminals, composed of $Zr_6O_4(OH)_4$ cluster and organic porphyrin ligand. [133]. Inspired by the work of Hu et al., Zhou et al. [122] successfully coupled C60 with PCN-224 under the driven by π-π interaction and physical adsorption via the strong binding characteristics (Fig. 12b). After coupling, the cubic shape of PCN-224 was basically maintained, and some nanoclusters C60 were observed on the cubic outer surface, C_{60} and PCN-224 could both absorb photons to generate excited e^-. Due to the relatively negative lowest unoccupied molecular orbital of PCN-224, the photogenerated e^- were transferred from PCN-224 to C60, and further entered into electrolyte to produce $O_2{\cdot}^-$. Simultaneously, the photogenerated h^+ of C60 were transferred to PCN-224 and were further removed by ITO electrons. Therefore, the donor-acceptor system constructed in PCN-224 and C_{60} facilitated the photogenerated electron transformation and suppressed carrier recombination (Fig. 12c). In the end, the team took advantage of the carboxyl terminus of PCN-224 as an efficient binding site for biomolecules to obtain a highly selective and sensitive PEC sensor C_{60}@PCN-224. They used nano-hybrids as probes and nanobodies as recognition unit to detect S100B and obtained considerable sensing performance.

Peng et al. [123] also did a research on the use of PCN-224 in PEC sensors for p-arsanilic acid (p-ASA). They used solvothermal method to in-situ grow PCN-224 on the surface of graphene oxide (GO), and used the formation of Zr-O-As from the coordination between PCN/rGO and p-ASA to construct the PEC sensor (Fig. 12d). Differently, the PCN-224/rGO nanocomposite photoelectrode served as the photocathode. The organic porphyrin ligands in PCN-224 were considered as light-harvesting elements. Under the light excitation, e^- was pumped from the valence band (HOMO) of

PCN-224 to the conduction band (LUMO). During this process, the dissolved O_2 might be reduced to superoxide radicals ($O_2\cdot^-$) by photogenerated e^-, thereby promoting the cathodic photocurrent. As can be seen from the mechanism diagram (Fig. 12e), as an adsorbate, p-ASA adjusted the energy band position of the PCN/rGO, weaken the electric field strength, and short the distance of the depletion layer. Of course, the photo-generated e^- could more easily cross the weaker interfacial electric field over a shorter depletion layer to reduce O_2, which generated increased photocurrent. Therefore, the composite achieved high PEC signal.

5. Stability, reproducibility and reusability of MOFs-modified photoelectrodes

Considering the practical application, the stability, reproducibility and reusability of MOFs and their derivatives-modified photoelectrodes are essential. At present, many studies have evaluated the stability, reproducibility and reusability (Table 3). Generally, stability can be evaluated from two aspects: structural stability and performance stability. Firstly, it is important to know whether the photoelectrodes can maintain their initial structures during the photo-electrocatalysis process. Li et al. [115] studied the X-ray diffraction pattens (XRD) and XPS of the photoelectrodes before and after the reactions, and found that the crystal phase and composition hardly changed after 3 cycles. In another study, Dong et al. [66] evaluated the structural stability of the photoelectrode more comprehensively by testing the SEM, TEM, and XRD after the reaction. They observed no obvious morphology and phase structure changes, which indicated that the MOFs-based core/shell nanocomposites had excellent stability. The enhanced stability is believed to be derived from the ultra-thin MOFs film and the tight connection between MOFs and inorganic semiconductors. It can be seen that the irradiation and bias in the photoelectric catalytic process have little effect on the main structure of MOFs and their derivatives-modified photoelectrodes. Secondly, the leaching concentration of metal ions in MOFs photoelectrodes can also reflect the difference in structural stability. For example, Cui et al. [116] found that the Fe element leached from the electrolyte only accounted for 1.33% after 180 min of constant working through inductively coupled plasma optical emission spectrometry (ICP-OES). The results indicated that MIL-100(Fe) exhibited low corrosion or etching after reactions, further indicating that MIL-100 (Fe) possesses a good stability during the photo-electrocatalysis process.

On the other hand, performance stability is a key issue in evaluating the further application of photoelectrodes. Photoelectrodes avoid the inconvenient recovery and declining recovery rate of the powder catalyst. And the performance stability is usually reflected by the long-term photocurrent curve, the cyclic switching experiment curve and the cyclic voltammetry curve. The photoelectrode developed by Zhang et al. [118] maintained 95.6% of the photocurrent signal after being stored at 4 °C for 3 weeks. The C60@PCN-224 photoelectrode constructed by Zhou et al. [122] maintained 89.82% of the initial photocurrent signal even after 1 month, which both showed satisfactory stability. Similar results have been published in many other works [81,112,134]. In addition, Feng's research team [135] carried a cycle switch experiment of MOF-derived In_2O_3@g-C_3N_4 photoelectrodes. Under ten on/off irradiation cycles, no noticeable signal changes were observed in the photocurrent response, and the reading was stable. The stability of the working electrode prepared by Fiaz et al. [136] was evaluated by repeating 50 cycles of cyclic voltammetry (CV) test. The CV curves of the 1st to 50th cycle overlapped with each other, with only negligible slight changes. In addition to stability, the evaluation of reproducibility often appears in the research of PEC sensors. To study this, Cao et al. [89] prepared ten identical photoelectrodes by using the same batch of MOF-derived CuO materials, and evaluated the reproducibility of PEC sensors through ten parallel experiments. The relative standard deviation (RSD) of the response photocurrent was 4.5%, indicating that the PEC sensor had good reproducibility. And the RSD in other similar studies are all less than 5% [86,119,121].

From the perspective of long-term industrial applications, the reusability of MOFs and their derivatives-modified photoelectrodes is another prominent issue to be considered. As mentioned above, in most cases, the prepared photoelectrodes are very stable and can be used to repeatedly treat organic pollutants. For example, in the study of Jia et al. [109] after completing 8 cycles degradation experiments, the degradation rate of the ZIF-8/NF-TiO_2 photoelectrode on sulfamethazine remained 90.4% of the initial degradation rate, and the RSD is 3.61%. Notably, it has also been observed that the catalytic activity of MOFs and their derivatives-modified photoelectrodes decrease with the increase of catalytic cycles, which is mainly due to the blockage of degradation intermediates to the active sites on the photoelectrode. Therefore, in the future exploration of photoelectrodes, cleaning and activation of the active sites on the photoelectrodes are the important direction.

Table 3
The stability, reproducibility, and reusability of MOFs and their derivatives-modified photoelectrodes.

Photoelectrode	Stability	Reproducibility/RSD RS DDD RSD	Reusability/P-IP Photocurrent signal	Refs.
ZnCdS@MoS_2	NA	7 parallel/5.20%	3 weeks/95.60%	[118]
C_{60}@PCN-224	NA	6 parallel/2.54%	4 weeks/89.82%	[122]
In_2O_3@g-C_3N_4	10 cycles	5 parallel/3.10%	1 weeks/92.20%	[135]
MIL-68(In)-NH_2/MWCNT/CdS	20 cycles	5 parallel/1.40%	NA	[111]
Cu-BTC	NA	10 parallel/4.50%	4 weeks/93.60%	[89]
CdS/Eu-MOF	NA	6 parallel/2.10%	1 weeks/97.80%	[87]
Ti-MOF/Fe_2O_3	NA	NA	5 h/98.9%	[114]
Fe_2O_3:Ti/NH_2-MIL-101(Fe)	10 cycles	NA	NA	[66]
MOF-5	3 cycles	NA	NA	[53]
NH_2-MIL-125(Ti)/TiO_2	NA	6 parallel/4.70%	1 weeks/94.10%	[137]
CoNi-MOFs/$BiVO_4$	NA	NA	3 h/90.0%	[73]
Au/UiO-66(NH_2)/CdS	10 cycles	5 parallel/2.20%	1 weeks/93.00%	[121]
$[Ru(bpy)_3]^{2+}$@UiO-66	NA	10 parallel/4.33%	NA	[120]
ZIF-67/TiO_2-NTs	NA	5 parallel/2.90%	NA	[138]

[a)] RSD: the relative standard deviation.
[b)] P-IP proportion of initial photocurrent.
[c)] NA: Not available.

Table 4
Other samples published in previous papers or commercial products.

Photoelectrode	PEC application/η	Highlights	Refs.
TNTs-Ag/SnO_2-Sb	Degradation/68%–60 min	Three dimensions structure	[139]
TiO_2-$BiVO_4$-BP/RP	Degradation/96.5%–240 min	Multi-heterojunction	[140]
NI TiO_2, (111) NRs	Degradation/88.3%–120 min	Improve the adsorption capacity	[141]
α-Fe_2O_3@CeO_2	Degradation/88.6%–60 min	Core-shell heterojunction	[142]
BiOBr/ITO	Degradation/91.4%–180 min	Nanosheet arrays structure	[143]
Sn NP/GaN NW/Si	CO_2 reduction/201 μmol·$cm^{-2}h^{-1}$	Covalent Ga-C and Sn-O bonding	[144]
ZnPc/C_3N_4	CO_2 reduction/1.625 μmol·$cm^{-2}h^{-1}$	Band matching	[145]
M-TiO_2@ZnO	CO_2 reduction/62.4 μmol·$cm^{-2}h^{-1}$	p-n heterojunction	[146]
Ti/ZnO–Fe_2O_3	CO_2 reduction/258 μmol·$cm^{-2}h^{-1}$	layered double hydroxides derivative	[147]
Pt-TNT/Pt-RGO	CO_2 reduction/935 nmol·$cm^{-2}h^{-1}$	Deposit of precious metals	[148]
Fe_{FAL}:GaN NWs	Water splitting/306 μmol·$cm^{-2}h^{-1}$	Spatial confinement of GaN	[149]
TiO_2@Au_{25}/TiO_2	Water splitting/7.973 μmol·$cm^{-2}h^{-1}$	Core-shell structure	[150]
Cu.Sn-$ZnFe_2O_4$	Water splitting/NA	Cu-Sn dual ions gradient doping	[151]
Aux/GQDs/NP-TNTA	Water splitting/NA	Electrostatic self-assembly strategy	[152]
β-In_2S_3	Water splitting/NA	Surface-defective	[153]

[a)] NA: Not available.

6. Conclusion and outlooks

In recent years, the vigorous development in the field of MOFs has led to important progress in MOFs and their derivatives-modified photoelectrodes in host–guest structural engineering, electrode system design, and PEC applications. As shown in Table 4, the photo-electrocatalysis of other conventional semiconductors is often attributed to some unique structural characteristics, such as heterojunctions, shell-core structures, three-dimensional structure, energy band matching, metal doping and extended application of derivatives, etc., while MOFs and their derivatives can intensively achieve the above structural requirements. Therefore, MOFs and their derivatives-modified photoelectrodes have the potential to become a promising alternative to conventional photoelectrodes in photo-electrochemistry. The conclusions derived from the various literature sources can be stated as follows: (1) Due to the structural diversity and semiconductor-like characteristics of MOFs, MOFs-modified photoelectrodes have rich development strategies and exact feasibility. In addition, based on the controlled porosity and high surface area of MOFs or MOFs derivatives, MOFs-modified photoelectrodes can increase the electrolyte/electrode contact area. (2) Among the various photoelectrode forming methods, the method of coating materials to form photoelectrodes is relatively common, while the materials are likely to fall off from photo-electrode. On the contrary, the method of evolving materials to form photoelectrodes is more stable, but research results are relatively few because of the complex synthesis process. (3) Among various MOFs, MILs-modified photoelectrodes are more widely used in photo-electrochemistry, including indium-based, titanium-based, and iron-based. Among them, iron-based materials of MIL have gained particular attention, and they have performed well in sensor, water splitting, heavy metals decontamination and organic pollutants degradation. Note that, researches in MOFs-modified photoelectrodes are still in infancy, many efforts are required to construct MOFs-modified photoelectrode with excellent and stable PEC properties. Here are some key points:

1. From the perspective of the conductive substrate and the active catalytic site, it is necessary to continuously explore novel MOFs-based photoelectrodes. Apart from commonly conductive substrates such as TiO_2 and $BiVO_4$, other new semiconductors should also be considered to obtain highly photoelectric active MOFs photo-electrocatalyst with various nanostructure.
2. From the perspective of the construction of the electrode system, it is urgent to develop a more effective bonding method between host and guest, thereby boosting electron transfer, reducing the barrier characteristics, and improving quantum efficiency. Material modification techniques, surface interactions, and structural matching can all be considered as effective strategies for obtaining photo-electrodes with lower overpotential and higher photoelectric conversion efficiency. In addition, exploring photocathode can further enrich the construction of the electrode system.
3. From the perspective of cost and environmental sustainability, developing high-efficiency, non-toxic and rich in earth elements photoelectrodes is more in line with the needs of green development. Furthermore, adding the evaluation mechanism of intermediate products ecotoxicity and human toxicity is also more conducive to the practical significance of study.
4. From the perspective of mechanism discussion, the theoretical analysis of DFT, kinetic Monte Carlo simulation and microscopic dynamic model should be mastered. Among them, simulation predictions and kinetic models can help us to better understand the interface properties of photoelectrodes and the charge transport in multi-component structures, especially the generation, separation, and migration of carriers at the nanometer scale. DFT theoretical calculations can be used to define the possible photoelectrode structure, simulate the adsorption of electrolyte on the photoelectrode surface, and calculate the electronic and optical characteristics of the photoelectrode.
5. From the perspective and direction of future development, machine learning and big data seem to be well used in research of this direction. In the current field of photo-electrochemistry, MOFs exhibit good application prospects for PEC materials because of wide variety and outstanding characteristics. However, the application of MOFs and their derivatives-modified photoelectrodes are at the preliminary stage, so it is necessary to develop photoelectrodes efficiently. The use of machine learning to combine calculations and experiments seems to be a potential method. It avoids complex algorithms and unpredictable errors based on the first- principle algorithm. And it uses basic data such as element electronic structure as a prior knowledge to combine data with computer algorithms for predicting the photocatalyst activity. Specifically, the key factors that affect the apparent rate constant of photo-electrocatalysis are selected as feature selection, then the basic data of MOFs and common semiconductors are used to predict the regression problem, linear regression, Gaussian process regression, etc., are further used to analyze the properties of MOFs and their derivatives-modified photoelectrodes. Finally, experiments are conducted to preliminary verify the effectiveness of key factors based on regression analysis and the advantages of regression models.

Declaration of Competing Interest

The authors declare that they have no known competing financial interests or personal relationships that could have appeared to influence the work reported in this paper.

Acknowledgement

This work was supported by the National Natural Science Foundation of China [grant numbers 51878258, 41807125 and 51908561] and National Youth Foundation of China [grant numbers 52000064].

References

[1] W. Wang, Z. Zeng, G. Zeng, C. Zhang, R. Xiao, C. Zhou, W. Xiong, Y. Yang, L. Lei, Y. Liu, D. Huang, M. Cheng, Y. Yang, Y. Fu, H. Luo, Y. Zhou, Chem. Eng. J. 378 (2019) 122132–122142.
[2] Y. Yang, G. Zeng, D. Huang, C. Zhang, D. He, C. Zhou, W. Wang, W. Xiong, B. Song, H. Yi, S. Ye, X. Ren, Small (2020) 2001634–2001645.
[3] X. Li, K. Cui, Z. Guo, T. Yang, Y. Cao, Y. Xiang, H. Chen, M. Xi, Chem. Eng. J. 379 (2020) 122324–122337.
[4] R. Passalacqua, S. Perathoner, G. Centi, J. Energy Chem. 26 (2017) 219–240.
[5] M. Cheng, Y. Liu, D. Huang, C. Lai, G. Zeng, J. Huang, Z. Liu, C. Zhang, C. Zhou, L. Qin, W. Xiong, H. Yi, Y. Yang, Chem. Eng. J. 362 (2019) 865–876.
[6] P. Song, Z. Yang, H. Xu, J. Huang, X. Yang, F. Yue, L. Wang, Desalin. Water. Treat. (2014) 1–9.
[7] P. Song, Q. Song, Z. Yang, G. Zeng, H. Xu, X. Li, W. Xiong, J. Environ. Manage. 228 (2018) 336–345.
[8] H. Yu, L. Jiang, H. Wang, B. Huang, X. Yuan, J. Huang, J. Zhang, G. Zeng, Small (2019) 1901008–1901038.
[9] W. Wang, Q. Niu, G. Zeng, C. Zhang, D. Huang, B. Shao, C. Zhou, Y. Yang, Y. Liu, H. Guo, W. Xiong, L. Lei, S. Liu, H. Yi, S. Chen, X. Tang, Appl. Catal., B 273 (2020) 119051–119063.
[10] Y. Yang, G. Zeng, D. Huang, C. Zhang, D. He, C. Zhou, W. Wang, W. Xiong, X. Li, B. Li, W. Dong, Y. Zhou, Appl. Catal., B 272 (2020) 118970–118983.
[11] I. Hod, M.D. Sampson, P. Deria, C.P. Kubiak, O.K. Farha, J.T. Hupp, ACS Catal. 5 (2015) 6302–6309.
[12] C. Zhang, L. Ai, J. Jiang, J. Mater. Chem. A 3 (2015) 3074–3081.
[13] L. Chi, Q. Xu, X. Liang, J. Wang, X. Su, Small 12 (2016) 1351–1358.
[14] H. Yu, B. Huang, H. Wang, X. Yuan, L. Jiang, Z. Wu, J. Zhang, G. Zeng, J. Colloid Interface Sci. 522 (2018) 82–94.
[15] C. Zhou, C. Lai, D. Huang, G. Zeng, C. Zhang, M. Cheng, L. Hu, J. Wan, W. Xiong, M. Wen, X. Wen, L. Qin, Appl. Catal., B 220 (2018) 202–210.
[16] C. Zhou, Z. Zeng, G. Zeng, D. Huang, R. Xiao, M. Cheng, C. Zhang, W. Xiong, C. Lai, Y. Yang, W. Wang, H. Yi, B. Li, J. Hazard. Mater. 380 (2019) 120815.
[17] A. Fujishima, K. Honda, Nature 238 (1972) 37–38.
[18] T.H. Jeon, M.S. Koo, H. Kim, W. Choi, ACS Catal. 8 (2018) 11542–11563.
[19] R. Sun, Z. Zhang, Z. Li, L. Jing, ChemCatChem 11 (2019) 5875–5884.
[20] X. Deng, R. Long, C. Gao, Y. Xiong, Curr. Opin. Electroche. 17 (2019) 114–120.
[21] R. Kaur, K.-H. Kim, A.K. Paul, A. Deep, J. Mater. Chem. A 4 (2016) 3991–4002.
[22] Z. Wang, H. Wang, Z. Zeng, G. Zeng, P. Xu, R. Xiao, D. Huang, X. Chen, L. He, C. Zhou, Y. Yang, Z. Wang, W. Wang, W. Xiong, Appl. Catal., B 267 (2020) 118700–118712.
[23] C.I.C. Chia-Chen Lee, Y.-T. Liao, K.-W. Wu, C.-C. Chueh, Adv. Sci. 6 (2019) 1801715–1801722.
[24] Y. Peng, Y. Li, Y. Ban, W. Yang, Angew. Chem. Int. Ed. Engl. 56 (2017) 9757–9761.
[25] T. Rodenas, I. Luz, G. Prieto, B. Seoane, H. Miro, A. Corma, F. Kapteijn, I.X.F.X. Llabres, J. Gascon, Nat Mater 14 (2015) 48–55.
[26] X. Wang, C. Chi, K. Zhang, Y. Qian, K.M. Gupta, Z. Kang, J. Jiang, D. Zhao, Nat Commun 8 (2017) 14460.
[27] J. Yu, W. Xiong, X. Li, Z. Yang, J. Cao, M. Jia, R. Xu, Y. Zhang, Microporous Mesoporous Mater. 290 (2019) 109642–109649.
[28] W. Xiong, Z. Zeng, X. Li, G. Zeng, R. Xiao, Z. Yang, Y. Zhou, C. Zhang, M. Cheng, L. Hu, C. Zhou, L. Qin, R. Xu, Y. Zhang, Chemosphere 210 (2018) 1061–1069.
[29] Y. Yu, X.J. Wu, M. Zhao, Q. Ma, J. Chen, B. Chen, M. Sindoro, J. Yang, S. Han, Q. Lu, H. Zhang, Angew. Chem. Int. Ed. Engl. 56 (2017) 578–581.
[30] J. Cao, S. Sun, X. Li, Z. Yang, W. Xiong, Y. Wu, M. Jia, Y. Zhou, C. Zhou, Y. Zhang, Chem. Eng. J. 382 (2020) 122802–122811.
[31] Y. Liu, D. Huang, M. Cheng, Z. Liu, C. Lai, C. Zhang, C. Zhou, W. Xiong, L. Qin, B. Shao, Q. Liang, Coord. Chem. Rev. 409 (2020) 213220–213238.
[32] C. Wang, Z. Xie, K.E. deKrafft, W. Lin, J. Am. Chem. Soc. 133 (2011) 13445–13454.
[33] H.-S. Wang, J. Li, J.-Y. Li, K. Wang, Y. Ding, X.-H. Xia, NPG Asia Mater. 9 (2017) 354–362.
[34] M. Zhao, Y. Wang, Q. Ma, Y. Huang, X. Zhang, J. Ping, Z. Zhang, Q. Lu, Y. Yu, H. Xu, Y. Zhao, H. Zhang, Adv. Mater. 27 (2015) 7372–7378.
[35] M. Zhao, Y. Huang, Y. Peng, Z. Huang, Q. Ma, H. Zhang, Chem. Soc. Rev. 47 (2018) 6267–6295.
[36] C. He, K. Lu, D. Liu, W. Lin, J. Am. Chem. Soc. 136 (2014) 5181–5184.
[37] K. Lu, C. He, W. Lin, J. Am. Chem. Soc. 136 (2014) 16712–16715.
[38] K. Lu, C. He, W. Lin, J. Am. Chem. Soc. 137 (2015) 7600–7603.
[39] M. Jian, H. Liu, T. Williams, J. Ma, H. Wang, X. Zhang, Chem. Commun. (Camb.) 53 (2017) 13161–13164.
[40] A.J. Clough, J.W. Yoo, M.H. Mecklenburg, S.C. Marinescu, J. Am. Chem. Soc. 137 (2015) 118–121.
[41] R. Dong, M. Pfeffermann, H. Liang, Z. Zheng, X. Zhu, J. Zhang, X. Feng, Angew. Chem. Int. Ed. Engl. 54 (2015) 12058–12063.
[42] L.J. Murray, M. Dinca, J.R. Long, Chem. Soc. Rev. 38 (2009) 1294–1314.
[43] X. Liao, H. Fu, T. Yan, J. Lei, Biosens. Bioelectron. 146 (2019) 111743–111752.
[44] L. Zhang, P. Cui, H. Yang, J. Chen, F. Xiao, Y. Guo, Y. Liu, W. Zhang, F. Huo, B. Liu, Adv. Sci. (Weinh.) 3 (2016) 1500243–1500248.
[45] W. Xiong, Z. Zeng, X. Li, G. Zeng, R. Xiao, Z. Yang, H. Xu, H. Chen, J. Cao, C. Zhou, L. Qin, Chemosphere 232 (2019) 186–194.
[46] C.-C. Chueh, C.-I. Chen, Y.-A. Su, H. Konnerth, Y.-J. Gu, C.-W. Kung, K.C.W. Wu, J. Mater. Chem. A 7 (2019) 17079–17095.
[47] H. Furukawa, K.E. Cordova, M. O'Keeffe, O.M. Yaghi, Science 341 (2013) 1230444–11123057.
[48] J. Cao, Z. Yang, W. Xiong, Y. Zhou, Y. Wu, M. Jia, S. Sun, C. Zhou, Y. Zhang, R. Zhong, Sep. Purif. Technol. 250 (2020) 117237–117246.
[49] W. Xiong, Z. Zeng, G. Zeng, Z. Yang, R. Xiao, X. Li, J. Cao, C. Zhou, H. Chen, M. Jia, Y. Yang, W. Wang, X. Tang, Chem. Eng. J. 374 (2019) 91–99.
[50] Y.-T. Liao, V.C. Nguyen, N. Ishiguro, A.P. Young, C.-K. Tsung, K.C.W. Wu, Appl. Catal., B 270 (2020) 118805–118817.
[51] Y.-T. Liao, B.M. Matsagar, K.C.W. Wu, A.C.S. Sustain, Chem. Eng. 6 (2018) 13628–13643.
[52] H. Konnerth, B.M. Matsagar, S.S. Chen, M.H.G. Prechtl, F.-K. Shieh, K.C.W. Wu, Coord. Chem. Rev. 416 (2020) 213319–213343.
[53] C. Hou, J. Peng, Q. Xu, Z. Ji, X. Hu, Rsc Adv. 2 (2012) 12696–12699.
[54] C. Hou, Q. Xu, J. Peng, Z. Ji, X. Hu, Chemphyschem 14 (2013) 140–144.
[55] X. Sun, Y. Li, J. Dou, D. Shen, M. Wei, J. Power Sources 322 (2016) 93–98.
[56] X. Deng, R. Li, S. Wu, L. Wang, J. Hu, J. Ma, W. Jiang, N. Zhang, X. Zheng, C. Gao, L. Wang, Q. Zhang, J. Zhu, Y. Xiong, J. Am. Chem. Soc. 141 (2019) 10924–10929.
[57] Q. Ma, H. Zhang, R. Guo, B. Li, X. Zhang, X. Cheng, M. Xie, Q. Cheng, Electrochim. Acta 283 (2018) 1154–1162.
[58] J.-Y. Huang, K.-Q. Zhang, Y.-K. Lai, Int. J. Photoenergy 2013 (2013) 1–19.
[59] J. Choi, H. Park, M.R. Hoffmann, J. Mater. Res. 25 (2011) 149–158.
[60] A. Kudo, Y. Miseki, Chem. Soc. Rev. 38 (2009) 253–278.
[61] D.-D. Qin, Y.-L. Li, T. Wang, Y. Li, X.-Q. Lu, J. Gu, Y.-X. Zhao, Y.-M. Song, C.-L. Tao, J. Mater. Chem. A 3 (2015) 6751–6755.
[62] E.S. Kim, H.J. Kang, G. Magesh, J.Y. Kim, J.W. Jang, J.S. Lee, ACS Appl. Mater. Inter. 6 (2014) 17762–17769.
[63] K.-H. Ye, Z. Chai, J. Gu, X. Yu, C. Zhao, Y. Zhang, W. Mai, Nano Energy 18 (2015) 222–231.
[64] D. Kong, J. Qi, D. Liu, X. Zhang, L. Pan, J. Zou, Trans. Tianjin Univ. 25 (2019) 340–347.
[65] C.Y. Toe, Z. Zheng, H. Wu, J. Scott, R. Amal, Y.H. Ng, Angew. Chem. Int. Ed. Engl. 57 (2018) 13613–13617.
[66] Y.-J. Dong, J.-F. Liao, Z.-C. Kong, Y.-F. Xu, Z.-J. Chen, H.-Y. Chen, D.-B. Kuang, D. Fenske, C.-Y. Su, Appl. Catal., B 237 (2018) 9–17.
[67] H. Song, Z. Sun, Y. Xu, Y. Han, J. Xu, J. Wu, T. Sun, H. Meng, X. Zhang, Sep. Purif. Technol. 228 (2019) 115764–115775.
[68] J. Zhou, A. Zhou, L. Shu, M.-C. Liu, Y. Dou, J.-R. Li, Appl. Catal., B 226 (2018) 421–428.
[69] G.Y. Zhang, Y.H. Zhuang, D. Shan, G.F. Su, S. Cosnier, X.J. Zhang, Anal. Chem. 88 (2016) 11207–11212.
[70] Y. Qiu, K. Yan, H. Deng, S. Yang, Nano Lett. 12 (2012) 407–413.
[71] C. Jiang, S.J.A. Moniz, M. Khraisheh, J. Tang, Chem. Eur. J. 20 (2014) 12954–12961.
[72] C. Liu, H. Luo, Y. Xu, Z. Zhang, Q. Liang, W. Wang, Z. Chen, Chem. Eng. J. 384 (2020) 123333–123342.
[73] S. Zhou, K. Chen, J. Huang, L. Wang, M. Zhang, B. Bai, H. Liu, Q. Wang, Appl. Catal., B 266 (2020) 118513–118546.
[74] T. Jiao, C. Lu, D. Zhang, K. Feng, S. Wang, Z. Kang, J. Zhong, Appl. Catal., B 269 (2020) 118768–118798.
[75] K.P. Pande, Y.S. Hsu, J.M. Borrego, S.K. Ghandhi, Appl. Phys. Lett. 33 (1978) 717–719.
[76] X. Li, S. Liu, K. Fan, Z. Liu, B. Song, J. Yu, Adv. Energy. Mater. 8 (2018) 1800101–1800108.
[77] F. Le Formal, N. Tétreault, M. Cornuz, T. Moehl, M. Grätzel, K. Sivula, Chem. Sci. 2 (2011) 737–743.
[78] J.Y. Kim, D.H. Youn, K. Kang, J.S. Lee, Angew. Chem. Int. Ed. Engl. 55 (2016) 10854–10858.
[79] R. Liu, Z. Zheng, J. Spurgeon, X. Yang, Energy Environ. Sci. 7 (2014) 2504–2517.
[80] J.E. Thorne, S. Li, C. Du, G. Qin, D. Wang, J Phys Chem Lett 6 (2015) 4083–4088.
[81] W. Li, K. Wang, X. Yang, F. Zhan, Y. Wang, M. Liu, X. Qiu, J. Li, J. Zhan, Q. Li, Y. Liu, Chem. Eng. J. 379 (2020) 122256–122266.
[82] H. Yang, J. Bright, S. Kasani, P. Zheng, T. Musho, B. Chen, L. Huang, N. Wu, Nano Res. 12 (2019) 643–650.
[83] Y.X. Yugang Sun, Science 298 (2002) 2176–2179.
[84] G. Lu, S. Li, Z. Guo, O.K. Farha, B.G. Hauser, X. Qi, Y. Wang, X. Wang, S. Han, X. Liu, J.S. DuChene, H. Zhang, Q. Zhang, X. Chen, J. Ma, S.C. Loo, W.D. Wei, Y. Yang, J.T. Hupp, F. Huo, Nat Chem 4 (2012) 310–316.

[85] L. Kőrösi, S. Papp, S. Beke, B. Pécz, R. Horváth, P. Petrik, E. Agócs, I. Dékány, Appl. Phys. A 107 (2012) 385–392.
[86] Y. Wang, H. Yin, X. Li, G.I.N. Waterhouse, S. Ai, Biosens. Bioelectron. 131 (2019) 163–170.
[87] J. Gao, Y. Chen, W. Ji, Z. Gao, J. Zhang, Analyst 144 (2019) 6617–6624.
[88] R. Yang, X. Yan, Y. Li, X. Zhang, J. Chen, A.C.S. Appl, Mater. Inter. 9 (2017) 42482–42491.
[89] Y. Cao, L. Wang, C. Wang, D. Su, Y. Liu, X. Hu, Mikrochim. Acta 186 (2019) 481–490.
[90] G. Liu, Y. Li, Y. Xiao, D. Jia, C. Li, J. Zheng, X. Liu, Catal. Lett. 149 (2018) 870–875.
[91] S.H. Park, Y.-H. Cho, M. Choi, H. Choi, J.S. Kang, J.H. Um, J.-W. Choi, H. Choe, Y.-E. Sung, Surf. Coat. Technol. 259 (2014) 560–569.
[92] T. Tang, K. Li, Z. Shen, T. Sun, Y. Wang, J. Jia, J. Power Sources 301 (2016) 54–61.
[93] M. Zhang, J. Cheng, X. Xuan, J. Zhou, K. Cen, Chem. Eng. J. 322 (2017) 22–32.
[94] J. Cheng, X. Xuan, X. Yang, J. Zhou, K. Cen, Int. J. Hydrogen Energy 44 (2019) 21597–21606.
[95] W.M.A. El Rouby, M. Antuch, S.M. You, P. Beaunier, P. Millet, Int. J. Hydrogen Energy 44 (2019) 30949–30964.
[96] G. Jia, L. Liu, L. Zhang, D. Zhang, Y. Wang, X. Cui, W. Zheng, Appl. Surf. Sci. 448 (2018) 254–260.
[97] H. Han, F. Karlicky, S. Pitchaimuthu, S.H.R. Shin, A. Chen, Small 15 (2019) 1902771–1902777.
[98] R. Kaur, K.-H. Kim, A. Deep, Appl. Surf. Sci. 396 (2017) 1303–1309.
[99] S.K. Sharma, K. Kumar, A.K. Paul, Mater. Res. Express 6 (2019) 125050–125065.
[100] R. Tang, S. Zhou, Z. Yuan, L. Yin, Adv. Funct. Mater. 27 (2017) 1701102–1701113.
[101] W. Yang, X. Wang, W. Hao, Q. Wu, J. Peng, J. Tu, Y. Cao, J. Mater. Chem. B 8 (2020) 2363–2370.
[102] J. Wang, C. Xue, W. Yao, J. Liu, X. Gao, R. Zong, Z. Yang, W. Jin, D. Tao, Appl. Catal., B 250 (2019) 369–381.
[103] R. Tang, R. Yin, S. Zhou, T. Ge, Z. Yuan, L. Zhang, L. Yin, J. Mater. Chem. A 5 (2017) 4962–4971.
[104] C.-C. Wang, X. Wang, W. Liu, Chem. Eng. J. 391 (2020) 123601–123638.
[105] V. Mahajan, S. Mohapatra, M. Misra, Int. J. Hydrogen Energy 33 (2008) 5369–5374.
[106] S. Li, G. Zhang, D. Guo, L. Yu, W. Zhang, J. Phys. Chem. 113 (2009) 12759–12765.
[107] H. Li, Z. Chen, C.K. Tsang, Z. Li, X. Ran, C. Lee, B. Nie, L. Zheng, T. Hung, J. Lu, B. Pan, Y.Y. Li, J. Mater. Chem. A 2 (2014) 229–236.
[108] F. Zhang, P. Zhang, Q. Wu, W. Xiong, Q. Kang, D. Shen, Electrochim. Acta 247 (2017) 80–88.
[109] M. Jia, Z. Yang, H. Xu, P. Song, W. Xiong, J. Cao, Y. Zhang, Y. Xiang, J. Hu, C. Zhou, Y. Yang, W. Wang, Chem. Eng. J. 388 (2020) 124388–124401.
[110] W. Jiao, J. Zhu, Y. Ling, M. Deng, Y. Zhou, P. Feng, Nanoscale 10 (2018) 20339–20346.
[111] X. Zhang, T. Yan, T. Wu, Y. Feng, M. Sun, L. Yan, B. Du, Q. Wei, Biosens. Bioelectron. 135 (2019) 88–94.
[112] J.W. Yoon, D.H. Kim, J.-H. Kim, H.W. Jang, J.-H. Lee, Appl. Catal., B 244 (2019) 511–518.
[113] L. Shi, D. Benetti, F. Li, Q. Wei, F. Rosei, Appl. Catal., B 263 (2020) 118317–118350.
[114] C.-H. Li, C.-L. Huang, X.-F. Chuah, D. Senthil Raja, C.-T. Hsieh, S.-Y. Lu, Chem. Eng. J. 361 (2019) 660–670.
[115] M. Li, Y. Liu, C. Shen, F. Li, C.C. Wang, M. Huang, B. Yang, Z. Wang, J. Yang, W. Sand, J. Hazard. Mater. 389 (2020) (1898) 121840–121912.
[116] W. Cui, H. Bai, K. Qu, F. Wang, P. Guan, D. Xu, W. Fan, W. Shi, Energy Technology 7 (2019) 1801128–1801137.
[117] H. Wang, X. He, W. Li, H. Chen, W. Fang, P. Tian, F. Xiao, L. Zhao, Chem. Commun. (Camb.) 55 (2019) 11382–11385.
[118] X. Zhang, J. Peng, Y. Ding, D. Zheng, Y. Lin, Y. Chen, W. Gao, Sensor Actuat. B-Chem 306 (2020) 127552–127587.
[119] J. Dou, D. Li, H. Li, Q. Kang, J. Lu, D. Shen, Talanta 197 (2019) 138–144.
[120] Z. Wang, Z. Yan, F. Wang, J. Cai, L. Guo, J. Su, Y. Liu, Biosens. Bioelectron. 97 (2017) 107–114.
[121] T. Wu, T. Yan, X. Zhang, Y. Feng, D. Wei, M. Sun, B. Du, Q. Wei, Biosens. Bioelectron. 117 (2018) 575–582.
[122] Q. Zhou, G. Li, K. Chen, H. Yang, M. Yang, Y. Zhang, Y. Wan, Y. Shen, Y. Zhang, Anal. Chem. 92 (2020) 983–990.
[123] M. Peng, G. Guan, H. Deng, B. Han, C. Tian, J. Zhuang, Y. Xu, W. Liu, Z. Lin, Environ. Sci-Nano 6 (2019) 207–215.
[124] M.-D.C.G. Férey, C. Serre, F. Millange, J. Dutour, S. Surblé, I. Margiolaki, Science 309 (2005) 2040–2042.
[125] C. Hou, Q. Xu, Y. Wang, X. Hu, RSC Adv. 3 (2013) 19820–19824.
[126] Y. Chen, J. Vela, H. Htoon, J.L. Casson, D.J. Werder, D.A. Bussian, V.I. Klimov, J. A. Hollingsworth, J. Am. Chem. Soc. 130 (2008) 5026–5027.
[127] W. Xiong, G. Zeng, Z. Yang, Y. Zhou, C. Zhang, M. Cheng, Y. Liu, L. Hu, J. Wan, C. Zhou, R. Xu, X. Li, Sci. Total Environ. 627 (2018) 235–244.
[128] X.C. Huang, Y.Y. Lin, J.P. Zhang, X.M. Chen, Angew. Chem. Int. Ed. Engl. 45 (2006) 1557–1559.
[129] B. Jia, P. Cao, H. Zhang, G. Wang, J. Mater. Sci. 54 (2019) 9466–9477.
[130] S.J. Jasmina Hafizovic Cavka, Unni Olsbye, Nathalie Guillou, Carlo Lamberti, Silvia Bordiga, Karl Petter Lillerud, J. Am. Chem. Soc., 130 (2008), pp. 13850–13851.
[131] J. Cao, Z.-H. Yang, W.-P. Xiong, Y.-Y. Zhou, Y.-R. Peng, X. Li, C.-Y. Zhou, R. Xu, Y.-R. Zhang, Chem. Eng. J. 353 (2018) 126–137.
[132] S. Ma, H.-C. Zhou, J. Am. Chem. Soc. 128 (2006) 11734–11735.
[133] T. Li, P. Hu, J. Li, P. Huang, W. Tong, C. Gao, Colloid Surface A 577 (2019) 456–463.
[134] Z. Jiao, J. Zheng, C. Feng, Z. Wang, X. Wang, G. Lu, Y. Bi, ChemSusChem 9 (2016) 2824–2831.
[135] Y. Feng, T. Yan, T. Wu, N. Zhang, Q. Yang, M. Sun, L. Yan, B. Du, Q. Wei, Sensor Actuat. B-Chem 298 (2019) 126817–126824.
[136] M. Fiaz, M. Athar, ChemistrySelect 4 (2019) 8508–8515.
[137] D. Jin, Q. Xu, L. Yu, X. Hu, Microchimica Acta 182 (2015) 1885–1892.
[138] Q. Zhang, F. Zhang, L. Yu, Q. Kang, Y. Chen, D. Shen, Mikrochim. Acta 187 (2020) 244–252.
[139] H. He, S. Sun, J. Gao, B. Huang, T. Zhao, H. Deng, X. Wang, X. Pan, J. Hazard. Mater. 398 (2020) 122805–122815.
[140] Y. Wang, J. Wu, Y. Yan, L. Li, P. Lu, J. Guan, N. Lu, X. Yuan, Chem. Eng. J. 403 (2021) 126313–126322.
[141] J. Zhang, B. Tang, G. Zhao, Appl. Catal., B 279 (2020) 119364–119372.
[142] S. He, C. Yan, X.-Z. Chen, Z. Wang, T. Ouyang, M.-L. Guo, Z.-Q. Liu, Appl. Catal., B 276 (2020) 119138–119149.
[143] Y. Ling, Y. Dai, J. Zhou, J. Colloid Interface Sci. 578 (2020) 326–337.
[144] B. Zhou, X. Kong, S. Vanka, S. Cheng, N. Pant, S. Chu, P. Ghamari, Y. Wang, G. Botton, H. Cuo, Z. Mi, Energy Environ. Sci. 12 (2019) 2842–2848.
[145] J. Zheng, X. Li, Y. Qin, S. Zhang, M. Sun, X. Duan, H. Sun, P. Li, S. Wang, J. Catal. 371 (2019) 214–223.
[146] B. Han, J. Wang, C. Yan, Y. Dong, Y. Xu, R. Nie, H. Jing, Electrochim. Acta 285 (2018) 23–29.
[147] S. Xia, Y. Meng, X. Zhou, J. Xue, G. Pan, Z. Ni, Appl. Catal., B 187 (2016) 122–133.
[148] M. Zhang, J. Cheng, X. Xuan, J. Zhou, K. Cen, ACS Sustain. Chem. Eng. 4 (2016) 6344–6354.
[149] B. Zhou, P. Ou, R.T. Rashid, S. Vanka, K. Sun, L. Yao, H. Sun, J. Song, Z. Mi, iScience 23 (2020) 101613–101633.
[150] S. Huo, Y. Wu, C. Zhao, F. Yu, J. Fang, Y. Yang, Ind. Eng. Chem. Res. 59 (2020) 14224–14233.
[151] Y. Lan, Z. Liu, Z. Guo, M. Ruan, Y. Xin, J. Colloid Interface Sci. 552 (2019) 111–121.
[152] W.J. Song, Talanta 170 (2017) 74–80.
[153] Y. Gao, S. Zhang, X. Bu, Y. Tian, Catal. Today 327 (2019) 271–278.